Prediction of the performance of regrind/flotation circuits using laboratory tests and quantitative mineralogical information

Submitted by Graham Davey to the University of Exeter

as a thesis for the degree of

Masters by Research in Mining and Minerals Engineering

In October 2017

I certify that all material in this thesis which is not my own work has been identified and that no material has previously been submitted and approved for the award of a degree by this or any other University.

Signature: ……..

Abstract

Three different regrind circuits were studied to assess whether it possible to predict the performance of the regrind circuits and the subsequent enrichment process. Process audits were conducted on one iron ore regrind circuit and two base metal regrind circuits to determine the performance of the regrind mills, classification equipment and either magnetic separation or froth flotation enrichment. Both laboratory grinding and enrichment tests were conducted to assess the suitability of currently available tests to predict the performance of the associated regrind circuit and enrichment. Simulated particle breakage of the regrind feed particles was also assessed using automated mineralogy and tessellation of the particles. The simulated mill product was then manipulated to simulate a downstream classification and enrichment process.

The laboratory methods and simulation showed good correlation with both the regrinding and enrichment phases for the iron ore regrind circuit. It was concluded that either method was suitable for iron ore regrind circuit design or optimization.

Due to the complexity of the base metal mineralogy and the flotation process after the regrind circuits it was more difficult to predict the performance of the base metal regrind circuits. The laboratory regrind tests showed good correlation for one circuit. The simulated breakage data provided a poor correlation for the product size distribution compared to the audit data, resulting in poor correlation of the liberation data. It was concluded that the simulated breakage, at very fine grind sizes required a modified method.

Contents

List of Figures

List of Tables

List of Abbreviations and Acronyms

Abbreviation / Acronym	Definition
SMD	Stirred Media Detritor
VTM	Vertimill
LIMS	Low Intensity Magnetic Separator
AG	Autogenous Grinding
SAG	Semi Autogenous Grinding
VPA	Vertical Pressure Air (Filter Press)
NRAB	Northlands Resources AB (Swedish Company)
XRF	X-Ray Fluorescence
QEMSCAN	Quantitative Evaluation of Minerals by SCANning electron microscopy
SEM	Scanning Electron Microscope
SDD	Silicon Drift Droplet
EDS	Electronic Backscatter Detector
PMA	Particle Mineral Analysis
pH	potential of Hydrogen
km	Kilometre
m	Metre
mm	Millimetre
µm	Micron
g	Gram
ml	Millilitre
t/m^3	Tonne / cubic metre
g/mt	Gram / metric tonne
g/l	Gram / litre
kPa	Thousand Pascals
kV	Thousand Volts
T	Tesla
Mtpa	Million tonnes per annum
mtph	metric tonnes per hour
kW	Thousand Watts
U/F	Underflow (Hydrocyclone)

O/F	Overflow (Hydrocyclone)
K_m	Volume magnetic susceptibility of a mixed particle
K_0	Volume magnetic susceptibility of pure magnetite
KAX	Potassium Amyl Xanthate
H_3BO_3	Boric acid
Ag	Silver
Cu	Copper
Fe	Iron
MgO	Magnesium Oxide
Pb	Lead
S	Sulphur
Sb	Antimony
SiO_2	Silica
Zn	Zinc

1 Introduction

1.1 Background

The aim of this study is to improve the ability of the metallurgist or plant designer to determine the optimum regrind size for an orebody based on both the properties of the orebody minerals assembly and the subsequent downstream mineral concentration technique. Most current orebodies and those that will be treated in the future involve fine or ultrafine regrinding. This is largely due to the exhaustion of the easier to process orebodies since the start of large scale mineral processing.

Due to the complexity of modern mineral processing plants and the great expense involved in the preparation of test samples for a feasibility study, the importance of developing methods to minimize sample quantity, the time taken to conduct tests and at the same time generate accurate data for process design and equipment selection is of great consequence. Based on industry values the preparation of a feasibility study costs around 5% of the total project cost (Harper 2008). For a large project such as the Constantia copper project in Peru with a total project cost of US$ 1.75 billion the feasibility study costs would be in the region of US$85 million (Kloln et al. 2016).

Most mineral processing plants involve a regrind stage, this is normally a size reduction step which is after a primary concentration step. Normally a primary concentration, at a coarser particle size, is performed to reduce the quantity of material requiring grinding to a finer particle size, this not only reduces the energy required but also the reagent consumption which is normally higher with finer

particles, which have a greater surface area. The grind size selected for the regrind step is then normally determined based on the optimum economic grade and recovery for the main economic mineral in the orebody. This is often a complex process and is related to a number of factors (Johnson 2006), including concentrate value (both payable elements and penalty elements), reagent cost, location power cost, smelting or leaching cost and concentrate shipping cost.

Due to the research and development of improved fine and ultrafine grinding mill technologies, the practicalities and economics of grinding to fine sizes have improved. Since the mid 1990's many stirred regrind mills have been installed around the world to regrind most types of complex mineral assemblies. For this reason, the research conducted will only involve stirred grinding mills rather than tumbling ball mills.

1.2 Outline of the Testwork

Two mineral processing concentrators were selected as examples containing modern regrinding processes. The concentrator flowsheets are explained and the sampling techniques used to audit the regrind section are detailed.

For the Northlands concentrator selected audit samples were used to conduct laboratory milling and magnetic enrichment testwork for comparison with the audit samples. For the Garpenberg concentrator selected audit samples were used for laboratory milling and flotation testwork.

Both the Northlands and Garpenberg audit samples were analysed using a QEMSCAN automated mineralogy system to generate liberation data for the various streams within the flowsheet. The QEMSCAN analysis also provided information on the particle size and mineralogical makeup of the feed, concentrate and tailings samples from the enrichment stage.

The mineralogical maps generated by the automated mineralogy system were then used for simulated breakage analysis using a computer based scientific image analysis program. The simulated fractured particle images could then be measured and analysed using their mineralogical profile.

The results from the size analysis, metallurgical testing, mineralogical analysis and simulated fracture were assessed using various techniques.

The first stage for the Northlands analysis results was to compare the laboratory metallurgical tests, including mill and enrichment with the results from the concentrator audit. This involved the comparison of size analysis, chemical assay and mineralogical data.

The second stage for the Northlands samples was the simulation of the regrind circuit using the mineralogical map of the feed particles and fracturing the particles using a computer model. The simulated mill product particles could then be magnetically enriched using the mineralogical profile data of the fractured particles and a simple separator model. This was again compared to the values generated from the plant audit.

The Garpenberg audit samples were again compared to the laboratory milling and flotation test samples generated from the laboratory metallurgical tests, involving size analysis, chemical assay and mineralogical data.

The mineralogical map data was then modelled using the same simulated fracture process. Multiple simulations were conducted to assess the impact of the tessellation size and the subsequent liberation of the fractured particles. The size analysis and liberation data for the simulated fractured particles was compared to the audit size data.

1.3 Regrinding and Enrichment

There is currently a lack of understanding about the required degree of regrind of enrichment products to produce a satisfactory grade and recovery for complex base and precious metal deposits. Currently, to determine the required grind size to obtain optimum liberation it is necessary to conduct laboratory flotation or other enrichment tests, then grinding tests followed by further flotation or enrichment tests. This becomes a major concern due to the mass of sample required when testing low grade ore deposits.

A typical copper project with a 0.5% Cu ore, using a 2000 g flotation sample, would only generate around 80-150 g of rougher concentrate. With many current and future projects, even this feed grade is at the higher end, a lower feed grade would result in even less concentrate for subsequent regrind testing. This sample mass is too small for any regrind and flotation test combination, which typically require a minimum of 500 g. If it were possible to use a testing procedure requiring

a smaller sample or automated mineralogy, to replace the current testing, this would avoid the need for larger batch flotation tests or even pilot plant testing.

The possible use of automated mineralogy to generate optimum first pass concentrate data would greatly reduce the possible errors in the selection of grinding mills and flotation cells. By using a model, developed to predict the breakage of the locked concentrate particles, the quantity and type of particles generated by a regrind mill could be calculated (Vassiliev et al. 2008). These particles could then be modelled using a concentration device model to predict the overall optimum grade and recovery. This approach would still require lab testing to generate data not predicted by the model, this could include data such as rate kinetics, entrainment, reagent type and reagent consumption.

To generate the model, sampling of existing operations would be required followed by the calculation of breakage data. The database of concentration and grind data can then be used to generate a robust model and compare the expected flotation performance from laboratory tests with the actual results. It would also then be possible to calibrate the full scale milling process against a laboratory mill to provide a laboratory routine for future samples (Mazzinghy et al. 2017).

One issue with a modelling only approach is the lack of information this provides on the kinetics of the froth flotation process. The kinetics are affected by the mineralogy of the ore, the degree of liberation and the chemical environment of the slurry. The chemical environment can be influenced by the type of mill and the grinding media used and the flotation reagents. To assess the flotation kinetics it would be necessary to use a small flotation sample test such as the rapid flotation

test, Mineral Separability Indicator (Bradshaw and Vos 2013), or develop a similar test that could provide additional flotation kinetics data. The data from the flotation kinetics testing could be included in the model for the overall process.

Modelling of a magnetite separation process is generally simpler, this is due to the standardised response of magnetite particles to a magnetic field, compared to the complex response of a chalcopyrite particle in a flotation cell. The number of elements in a successful flotation enrichment is a magnitude greater than in a magnetic enrichment process. A number of models have been generated for wet Low Intensity Magnetic Separators (LIMS), however most have been tested using cobbing magnetic separator data (Parian et al. 2016). Cobbing or roughing magnetic separators are the first stage of separation and the grind size is relatively coarse, typically in the range 100-1000 microns. Limited study has been conducted around the finishing or cleaner magnetic separators, at this stage recovery is less important than gangue rejection to make a high-quality concentrate. Feed size to the finishing magnetic separators is often 100 microns or finer, many modern plants now grinding down to 50 microns or finer.

To check on the reliability of the model and ability to aid in future flowsheet development, it is proposed to include surveyed laboratory and pilot trials from existing flotation regrind circuits. These would be selected to cover a range of milling technologies to provide the widest use for the modelling and testing procedure.

The determination of the optimum regrind size is a function of the following elements:

1. Regrind mill type and performance
2. Enrichment method
    a. Flotation
    b. Magnetic
3. Assaying and analysis of the products
4. Modelling

Not all of these requirements will be covered in this thesis.

1.4 Regrinding

The number of stirred regrind milling technologies available to the process engineer have increased significantly over the last 20 years. The first type of stirred mill studied is the Metso Vertimill®, shown in Figure 1, or tower mill which is a screw type mill using steel media. Generally the Metso Vertimill® is a slower speed attrition mill and is always operated in closed circuit with typically a hydrocyclone array, although fine screens or screw classifiers are an alternative (Lichter and Davey 2002).

Figure 1: Metso Vertimill® Regrind Mill

The second type of mill studied is the Metso Stirred Media Detritor (SMD), Figure 2, which is a high speed fluidized media mill, which is often operated in open circuit with a classifier or thickener prior to the mill for density control (Lichter and Davey 2002). Typically, the Metso SMD is used for finer grinds to produce slurries with an 80% passing size of 45 microns or finer. Often the required product size is less than 80% passing 15 microns or finer for good liberation with a complex sulphide ore (Davey 2002).

Figure 2: Metso Stirred Media Detritor Regrind Mill

The operation of the mill, in closed or open circuit, is important due to the classification differences due to the distinct mineral properties within a typical ore. With a hydrocyclone the classification or cut size of the particles is partly determined by the density of the particles, denser particles will have a finer cut size and will preferentially report to the hydrocyclone underflow. The hydrocyclone underflow in a closed circuit grinding system is returned to the regrind mill so dense particles will typically have more passes through the mill. The density effect on the hydrocyclone will typically produce a bimodal or multimodal size curve affecting the operation of the downstream enrichment process.

This process is also affected by the type of mill and also the hardness of the minerals (Runge et al. 2013). Even the particle shape for a sample with the same size distribution and composition can have an effect on the downstream enrichment process (Vizcarra et al. 2011).

Mineral hardness or differences in mineral grindability can also affect the size distribution of the ground minerals, possible resulting in a bimodal size distribution and different or improved liberation. During grinding of a Chinese iron ore sample, it was found that magnetite ground in a laboratory stirred mill had greater liberation, compared to a lab ball mill. This was true even at the same 80% passing product size (Xiao et al. 2012).

1.5 Enrichment Process

All enrichment processes are affected by the comminution process and the subsequent liberation of the minerals within the ore. Two of the major enrichment processes used within the mining industry are froth flotation and magnetic separation. Both flotation and magnetic separation techniques can be affected by the comminution process, this can modify the liberation but in the case of flotation can also affect the pulp chemistry. Both enrichment processes have well defined and reliable laboratory testwork and equipment selection techniques.

Magnetic separation has the more beneficial test in terms of a small sample size and avoids the need of multiple tests for alternative reagent schemes, unlike flotation. The Davis tube test, the standard small scale magnetic separation test, uses around 20g of sample per test, often the assaying of the samples defines the sample size or if multiple runs are required, this is especially true for samples with either very high or low grades and when concentrate impurities are a significant factor in the concentrate quality or economic value. The magnetite enrichment process, grade and recovery, can often be well defined for a deposit with relatively

few Davis tube tests. However, measuring or predicting the level of impurities, an important factor in iron ore concentrates, may require a factor of 20 or more additional tests (Lishchuk et al. 2016).

The importance of the gangue rejection is vital to obtain a high-quality concentrate and most mineral processing concentrators have focused on processes to improve rejection of coarser low-density particles containing small quantities of magnetite. However, gangue recovery, via entrainment or entrapment, to the final concentrate is also a significant area of concern. When high concentrations of magnetite are present in the LIMS feed, as is always the case with the finishing stage, gangue recovery to the concentrate can be as high as 80-90%, especially with fine particles as shown in Figure 3 (Ersayin 2004).

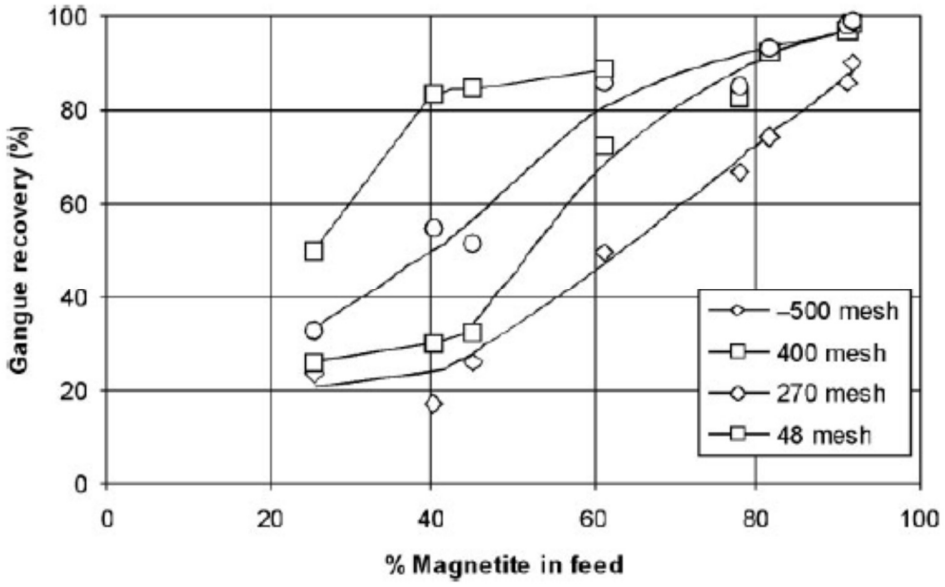

Figure 3: Gangue Recovery versus Magnetite Concentration in the Separator feed (Ersayin 2004)

As finer grinding is required at new iron ore concentrators or existing concentrators, due to more complex mineralogy, the magnetic response of fine

magnetite and gangue becomes more critical. Fine magnetite particles have a higher residual magnetism than coarser particles after magnetization, resulting in enhanced magnetic flocculation. Finer magnetite particles have a higher coercive force than coarser particles and as a result finer particles will form magnetic aggregates of a higher tensile strength than those formed from coarser particles (Dworzanowski 2012).

The main laboratory flotation test procedure is still batch laboratory flotation tests, often using a Metso or Denver D12 flotation machine, although other laboratory machines are available sometimes including complex impeller or automated scraper systems (Wood 2002). One major issue with laboratory flotation batch tests is the quantity of sample required which is normally a minimum of 500g but can be higher, especially if multi stage processing is required. Batch flotation tests tend to be sensitive to minor variations in operator technique, which is why automated froth removal or scraper systems have been developed.

Cleaning tests are particularly complicated and may require the use of locked cycle flotation tests. Locked cycle flotation tests involve feeding forward or recycling batch flotation test concentrate or tails to better replicate the full circuit. This has a significant effect on the sample quantities required, feed sample weight is unlikely to be less than 10kg.

Typically scale up batch test results to full scale continuous flotation cells or banks is relatively straight forward, although most engineers still use a scale up factor which is often poor defined and understood. Depending on the scale up

factor used the final plant can still be significantly undersized or oversized (Wills and Finch 2016).

The lab test will provide a good understanding of the reagents required for optimum flotation performance and the kinetics of the flotation performance can be calculated. Using flotation kinetics tests and process mineralogy it is possible to improve process design for the flotation circuit (Whiteman et al. 2015).

2 Sampling and Sample Testing

2.1 Introduction

Chapter 2 provides a detailed account of the two mineral processing concentrators selected as examples of modern regrinding processes. The concentrator flowsheets are explained and the sampling techniques used to audit the regrind section is detailed.

For the Northlands concentrator selected audit samples were used to conduct laboratory milling and magnetic enrichment testwork for comparison with the audit samples. For the Garpenberg concentrator selected audit samples were used for laboratory milling and flotation testwork.

Both the Northlands and Garpenberg audit samples were analysed using a QEMSCAN automated mineralogy system to generate liberation data for the various streams within the flowsheet. The QEMSCAN analysis also provided information on the particle size and mineralogical makeup of the feed, concentrate and tailings samples from the enrichment stage.

The mineralogical maps generated by the automated mineralogy system were then used for simulated breakage analysis using a computer based scientific image analysis program. The simulated fractured particle images could then be measured and analysed using their mineralogical profile.

2.2 Northlands Iron Ore Concentrator Regrind Circuit

The Northlands Resources Kaunisvaara operation in North-West Sweden was designed as a high capacity, yet low operating cost, state of the art iron ore

concentrator. The aim of the project was to produce a superior product by using a mix of both conventional and innovative mineral processing technology and techniques.

The Tapuli iron ore deposit is located in the Pajala area of North-West Sweden and is about 3.5 km North East from the similar Stora Sahavaara deposit. The current resources of the Tapuli are about 115 Mt of relatively low Fe grades, averaging around 26% Fe. The deposit occurs as a set of semi-continuous tabular bodies that dip 45-60 degrees to North West. A substantial part of the mineralization consists of breccia hosted magnetite bodies. The host rock sequence is (from hanging wall to footwall) quartzite, dolomitic marble, graphitic phyllite and mafic volcanic rock. The metasomatic skarns and magnetite overprint the dolomitic marble and phyllite. The sole ore mineral in Tapuli is magnetite with only trace amount of pyrite and pyrrhotite. The gangue consists of cliopyroxene, tremolite, actinolite, serpentine, and carbonates (Baker and Lepley 2010).

The Tapuli mine process comminution line consists of gyratory crushing followed by a Metso 34’ x 18.75’ autogenous grinding mill (no steel grinding media) with 11,600 kW drives and three (3) VTM-3000-WB METSO VERTIMILL® grinding mills. The AG mill feed is sized prior to the ROM stockpile, to produce both a ROM and a lump stock. This allows autogenous grinding performance to be maintained and stabilized during periods of feed size and hardness variation. The autogenous grinding mill will process a throughput rate of at least 761 metric tonnes per hour, from a feed size of 80% minus 200 mm to a target product size that averages at least 80% minus 300 microns. The AG mill is followed by rougher (cobbing)

magnetic separation and the resulting 341 metric tonnes per hour of pre-concentrate will report to secondary grinding. By rejecting a coarse cobbing tailings stream, secondary grinding energy is reduced and the tailings can be dry stacked, reducing tailings management costs.

The secondary Metso Vertimill® grind the cobbing or magnetic rougher concentrate to the optimised liberation size of 80% minus 35 to 40 microns. The product from the Metso Vertimill® can then pass to the final finishing magnetic separation. By careful selection of the Metso Vertimill® circuit it was possible to substantially reduce the secondary grinding energy compared to the use of conventional ball mills. Compared to alternative stirred mills trialed in iron ore circuits, operating costs were also significantly lower with high availability, which resulted in high plant productivity for the Metso Vertimill®.

After the Metso Vertimill® regrind mills, the regrind circuit product flowed to a final stage of wet magnetic separation, using 3 stage low intensity magnetic separators (LIMS). The cleaned magnetic concentrate was then dewatered and stockpiled ready for shipping to clients, the tails are combined with the primary cobbing tailings and were thickened and then pumped to the tailings dam. A simplified flowsheet is shown in Figure 4.

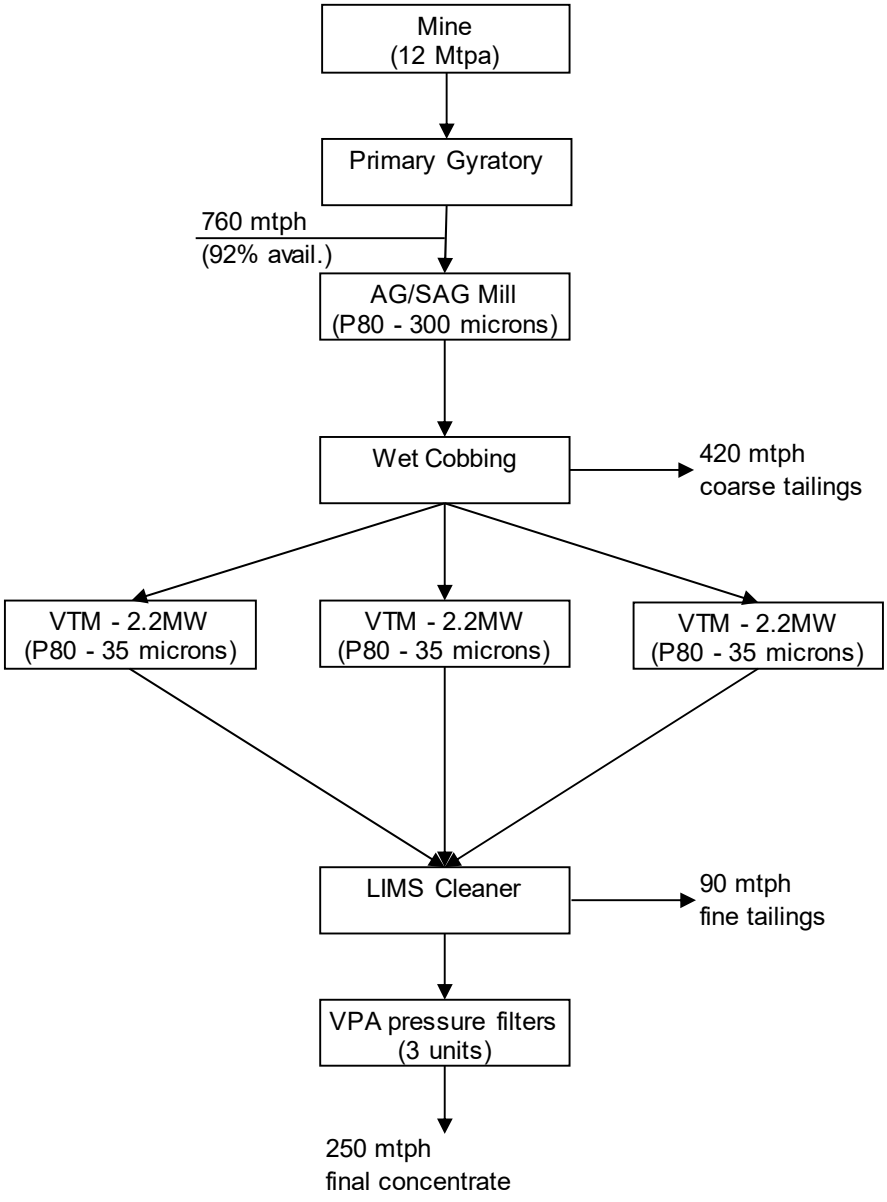

Figure 4: Simplified Northlands Resources (NRAB) Tapuli Flowsheet (approximately 12 Mtpa ore production)

The regrind circuit and final magnetic separators circuit contained several automatic sampling points and flow, density, pressure and power instrumentation devices.

The regrind circuit containing the three VTM-3000 mills were fed from the cobbing LIMS magnetic concentrate. The magnetic concentrate flowed by gravity to a 4-way flow splitter, which splits the slurry into 3 equal streams, one port of the splitter was blocked off.

Each separated feed stream flowed to the hydrocyclone feed sump, each mill having a separate sump, pumps and hydrocyclone array. The fresh feed, dilution water and the Metso Vertimill® discharge slurry combine in the sump and pumped to a hydrocyclone array, a 12-way array each with 11 hydrocyclones fitted. Each hydrocyclone was a FLSmidth Krebs GMax10-3226 unit, fitted with 50mm vortex finders.

The regrind Metso Vertimill® VTM1 and VTM2 were installed with an arrangement to allow feed to be pumped to the bottom of the mill, VTM3 was only fed to the top of the mill. The instrumentation and sampling points within the circuit are listed below. The circuit also had online XRF analysis which was used to collect samples for laboratory analysis, using the plant and XRF sub-samplers, however the XRF analyzers were not fully calibrated so online analysis results were not collected.

All plant instrumentation readings were transmitted to the control room and displayed in real time, the data was also saved in the plant data historian.

Table 1: List of Instrumentation Locations

Circuit Position	Type	Instrument	Auto. / Manual
Regrind Circuit Feed	Volumetric Flow	Radar Flow Meter	Automated
Regrind Circuit Feed	Slurry Density	Nucleonic Density	Automated
Regrind Circuit Feed	Sample	Online XRF analyser	Manual
Mill Power	Power Measure.	kW meter	Automated
Hydrocyclone Feed	Volumetric Flow	Radar Flow Meter	Automated
Hydrocyclone Feed	Slurry Density	Nucleonic Density	Automated
Hydrocyclone Feed	Sample	Hydrocyclone Port	Manual
Hydrocyclone Overflow	Sample	Online XRF analyser	Manual
Hydrocyclone Pressure	Pressure	Pressure Gauge	Automated
LIMS Product	Sample	Online XRF analyser	Manual
LIMS Tails	Sample	Online XRF analyser	Manual

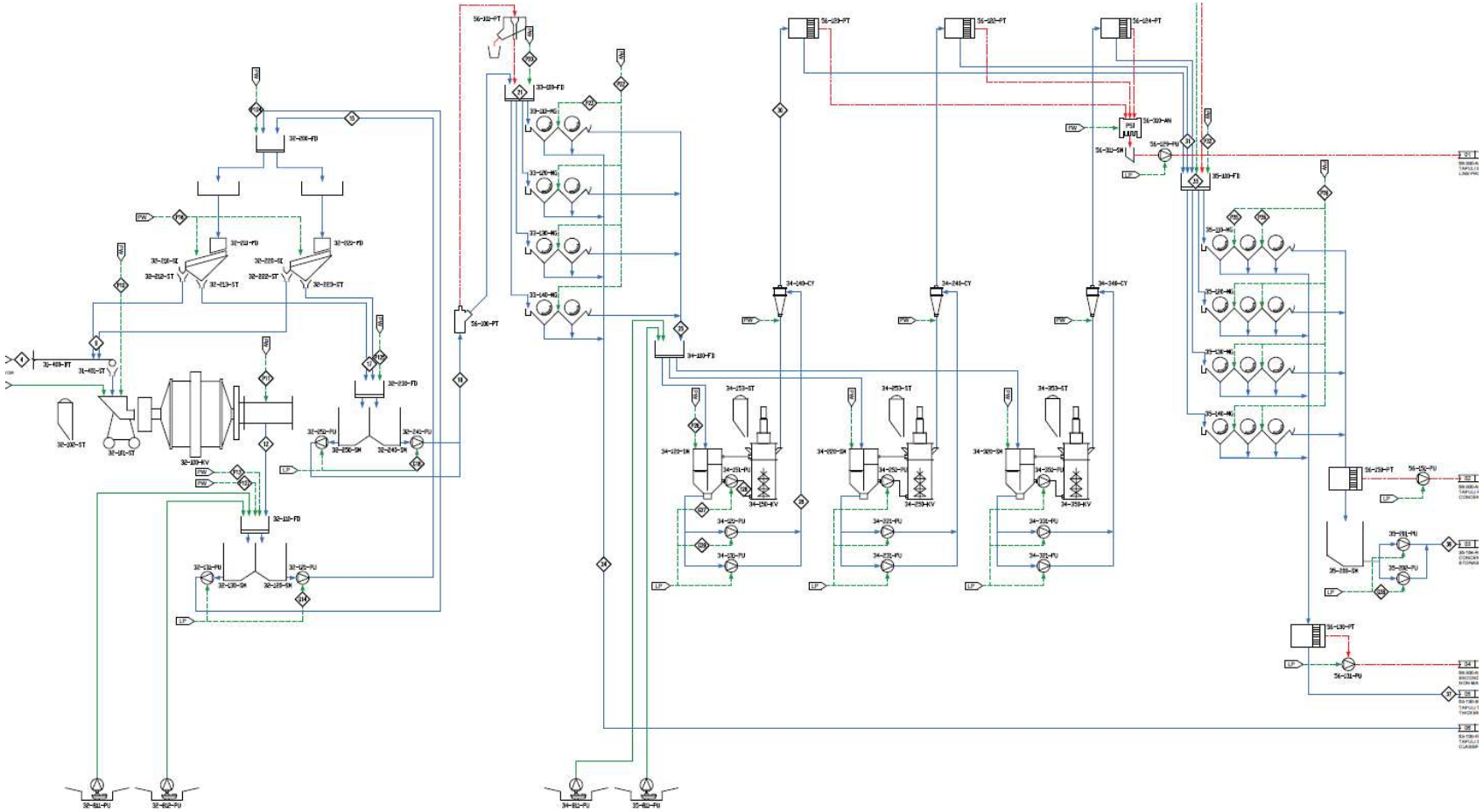

Figure 5: Detailed Tapuli Flowsheet with Automated Sampling Systems

All automated flow, density, power and pressure data was captured by the distributed control system. The values were then averaged over the sampling period and downloaded.

Table 2: List of Sample Locations / Collection Method

Circuit Position	Composition	Auto. / Manual
Regrind Circuit Feed (VTM1)	Composite 4 samples over 1 hour	Manual
Vertimill Discharge (VTM1)	Composite 4 samples over 1 hour	Manual
Hydrocyclone Underflow (VTM1)	Composite 4 samples over 1 hour	Manual
Hydrocyclone Overflow (VTM1)	Composite 4 samples over 1 hour	Manual
Regrind Circuit Feed (VTM2)	Composite 4 samples over 1 hour	Manual
Vertimill Discharge (VTM2)	Composite 4 samples over 1 hour	Manual
Hydrocyclone Underflow (VTM2)	Composite 4 samples over 1 hour	Manual
Hydrocyclone Overflow (VTM2)	Composite 4 samples over 1 hour	Manual
Regrind Circuit Feed (VTM3)	Composite 4 samples over 1 hour	Manual
Vertimill Discharge (VTM3)	Composite 4 samples over 1 hour	Manual
Hydrocyclone Underflow (VTM3)	Composite 4 samples over 1 hour	Manual
Hydrocyclone Overflow (VTM3)	Composite 4 samples over 1 hour	Manual
Regrind Circuit Feed	Composite 4 samples over 1 hour	Automated
Regrind Circuit Product	Composite 4 samples over 1 hour	Automated
LIMS Concentrate	Composite 4 samples over 1 hour	Automated
LIMS Tailings	Composite 4 samples over 1 hour	Automated

The hand samplers used were stainless steel samplers, selected for each stream based on the flow and particle size of the stream.

All survey samples were collected in plastic buckets and labelled before transferring to the onsite laboratory. Samples were then either analysed on site using standard mining screens and XRF analysis or filtered and packaged for shipping offsite for the specialized process analysis and testing. The samples for QEMCAN analysis were shipped to the Camborne School of Mines in the UK. The samples for Davis Tube testing and jar mill testing were shipped to the Metso York laboratory.

2.3 Northlands Sample Testing and Analysis

Davis tube tests were conducted on the LIMS feed sample collected from the Northlands survey to determine the magnetite and gangue recovery. A Davis tube test was also conducted on sample of the Metso Vertimill® regrind circuit feed which had been ground in a Metso jar mill to determine the effect of a batch laboratory mill compared to the industrial milling and magnetic separation circuit. The Metso jar mill procedure is detailed separately.

The Davis Magnetic Tube Tester consists of an extremely powerful electromagnet which can generate a magnetic field intensity of up to 0.4 Tesla, a glass separation tube and a motor driven agitation mechanism which is visually represented in Figure 6. The glass tube was positioned between the poles of the magnet at an angle of 45 degrees. Tests were conducted on the different samples and a range of magnetic intensities to determine the magnetite and gangue recovery. The test on the jar mill sample was run with a magnetic intensity of 0.1 Tesla to simulate the industrial LIMS that operate with a similar magnetic intensity. The test procedure required multiple runs to generate a

sufficient quantity of tailings for XRF analysis. The feed sample was fed in to the water filled tube whilst the tube was agitated and rotated. Any magnetic particles present in the product sample inside the tube were held by the magnetic force in the zone between the magnetic coil. The agitation resulted in a washing action removing any non-magnetic particles and allowing the non-magnetic particles to drop in to the discharge end of the tube. After a set period the agitation is stopped and the tailings / non-magnetic particles are flushed from the tube and collected, this process is then repeated for the magnetic sample after the magnet is turned off (Sepor 2010). The samples were dried and weighed and submitted for XRF analysis.

Figure 6: Davis Tube Tester

A sample of the Metso Vertimill® regrind circuit feed was ground using the Metso jar mill. The Metso jar mill test consists of a 203mm x 254mm steel jar rotated at 76% of critical speed. The slurry was at 65% solids w/w and the media used was a 19mm steel

ball charge. Individual tests were conducted for various time periods to generate a product size versus time curve. A time was then selected based on matching the jar mill product 80% passing size to the 80% passing size of the full-scale Northlands Metso Vertimill® circuit. A final test was then conducted at the calculated time to generate the sample for jar mill testing. Power was measured during the test runs so that the specific energy for the test could also be compared to the industrial circuit. Sizing of the product slurry was conducted using standard mining screens (Metso 2010).

XRF samples were prepared using the mix 5 g of dried and ground sample with 2.5 ml of a solution of Elvacite 2013 resin dissolved in acetone (200 g/l) in an agate pestle and mortar until a dry powder remains. This is loaded into a steel pressing die (40 mm diameter), then boric acid (H_3BO_3) is added as a backing material; the pellet is pressed in a Moore hydraulic press at 20 tonnes for 60 seconds, then ejected from the die. By performing upon one sample a qualitative scan with peak identification, and then utilising the fundamental parameters (FP) method to relate measured and theoretical intensities of detected elements and perform inter-element corrections, a determination of sample chemistry is made. Alternative peaks were selected for the iron analysis due to the high intensity peak detection.

2.4 Boliden Garpenberg Zn/Pb/Ag Concentrator Regrind Circuit

The second plant survey was conducted at Boliden Garpenberg, the aim being to study another type of stirred mill, the Metso Stirred Media Detritor (SMD) and a different enrichment technique.

Boliden Garpenberg is a large Ag / Pb / Zn with mine in central Sweden, the deposit also contains small quantities of copper.

The Boliden Garpenberg complex sulphide ore contains sphalerite, galena and chalcopyrite as the valuable sulphide minerals but with pyrite being the dominant sulphide mineral. The sphalerite has a high grade of iron (7--8 percent) in most ores. Accessory minerals are pyrrhotite, tetrahedrite and arsenopyrite. Gold is most often in amalgam but occurs sometimes as small inclusions in arsenopyrite. The gangue minerals are mainly quartz, sericite, dolomite, chlorite, felsitic chlorite and calcareous tuffites. The sulphur content is varying from 5 % to 40 % in the different ores (Bolin and Norén 1992).

The Garpenberg comminution and enrichment flowsheet consists of an autogenous grinding mill and pebble grinding mill circuit grinding to a flotation feed size of approximately 80% passing 85 to 100 microns. The primary grinding circuit also contains a gravity and flash flotation circuit to recover any free precious metals.

The product from the grinding circuit is pumped to the copper-lead flotation circuit, where a copper-lead-silver rich concentrate is produced. This then goes to a separate flotation section which produces separate copper-silver and lead concentrates.

The copper-lead circuit consists of a 4-cell flotation rougher flotation bank followed by a 3-cell scavenger bank. The rougher bank is further split to allow the concentrate from the first two cells to feed either the 1st cleaner bank or bypass to the second cleaner bank.

Cleaner flotation consists of three stages, 1st cleaner with 2 cells, 2nd cleaner with 2 cells and a single cell 3rd cleaner. Concentrate from the 3rd stage cleaner flows to the copper / lead separation circuit.

Both the 1st cleaner tails and the scavenger concentrate are pumped to the regrind circuit. The regrind circuit feed is first fed to an array of FLSmidth Krebs 250mm, 20-degree cone angle hydrocyclones, which are used to remove any particles already at or below the desired grind size and to maintain a higher and constant density to the SMD grinding mill. The hydrocyclones were operating with a relatively low pressure, 50 kPa, due to issues with the feed pump. However, a suitable split was still produced by the hydrocyclone and the feed to the SMD was at a low but adequate density.

The hydrocyclone array underflow stream flowed by gravity to the SMD, the slurry was diluted further by a process water line. The SMD discharge was then combined with the hydrocyclone array overflow stream and pumped back to the flotation conditioning tank at the head of the rougher-scavenger bank.

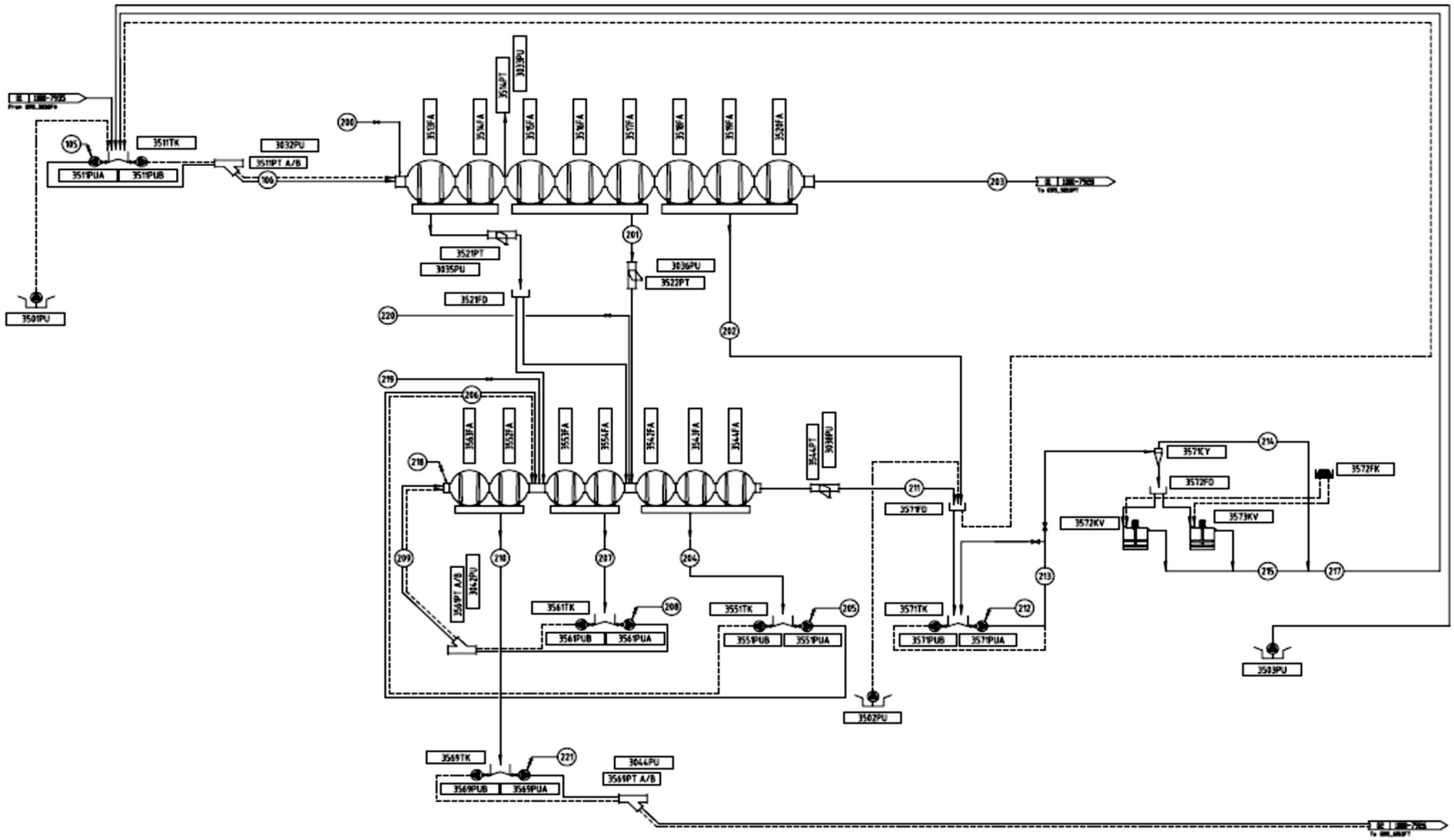

Figure 7 : Garpenberg Zinc Flotation Circuit Process Flow Diagram

Due to the complexity of the recycle streams it was decided to check the flotation performance of the regrind circuit by using a laboratory flotation test. A test would be conducted on the regrind circuit feed and then a separate flotation test using the same conditions on the combined product from the regrind circuit, details of the laboratory flotation are listed after the zinc survey section.

The zinc circuit consists of a 5-cell flotation rougher flotation bank followed by a 3-cell scavenger bank. The rougher bank is again split to allow the concentrate from the first two cells to feed either the 1st cleaner bank or bypass to the second cleaner bank.

Cleaner flotation consists of three stages, 1st cleaner with 3 cells, 2nd cleaner with 2 cells and 3rd cleaner with 2 cells. Concentrate from the 3rd stage cleaner flows to the zinc concentrate dewatering circuit.

Both the 1st cleaner tails and the scavenger concentrate are pumped to the regrind circuit. The regrind circuit feed is first fed to an array of FLSmidth Krebs 250mm, 20-degree cone angle hydrocyclones, which are used to remove any particles already at or below the desired grind size and to maintain a higher and constant density to the SMD grinding mill. The hydrocyclones were operating with a pressure of 90 kPa.

The milling circuit consists of 2 Metso SMD grinding mills, one is normally operational with one in standby mode. The mills are fitted with an automated media addition system which maintains a constant power draw by adding media as media is consumed by the grinding process. The media used at Garpenberg is 4mm diameter, 3.6 t/m^3 specific gravity, ceramic grinding beads. The ceramic grinding beads are added automatically based on a mill power draw set point.

The hydrocyclone array underflow stream flows by gravity to the SMD, the slurry is then diluted further by a process water line. The SMD discharge was then combined with the hydrocyclone array overflow stream and pumped back to the flotation conditioning tank at the head of the rougher-scavenger bank.

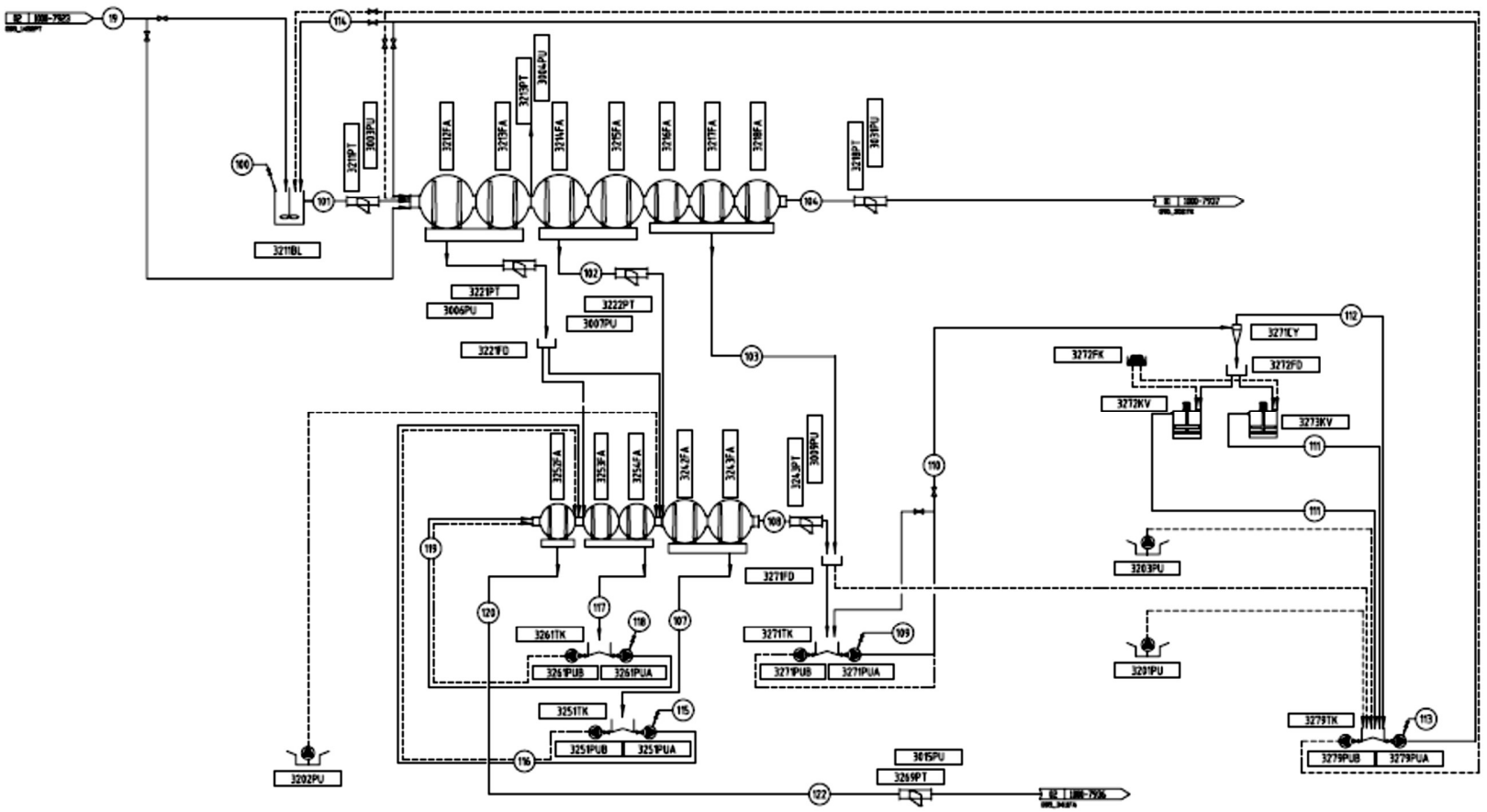

Figure 8 : Garpenberg Pb/Cu Flotation Circuit Process Flow Diagram

Table 3: List of Instrumentation Locations

Circuit Position	Type	Instrument	Automated / Manual
Mill Power	Power Measure.	kW meter	Automated
Hydrocyclone Feed	Volumetric Flow	Radar Flow Meter	Automated
Hydrocyclone Feed	Slurry Density	Nucleonic Density	Automated
Hydrocyclone Feed	Sample	Hydrocyclone Port	Manual
Hydrocyclone Pressure	Pressure	Pressure Gauge	Automated

All automated flow, density, power and pressure data was captured by the distributed control system.

Table 4: List of Sample Locations / Collection Method

Circuit Position	Composition	Automated / Manual
CuPb scavenger concentrate	Composite 4 samples over 1 hour	Manual
CuPb Cleaner 1 tails	Composite 4 samples over 1 hour	Automated
CuPb Hydrocyclone feed	Composite 4 samples over 1 hour	Manual
CuPb Hydrocyclone overflow	Composite 4 samples over 1 hour	Manual
CuPb Hydrocyclone underflow	Composite 4 samples over 1 hour	Manual
CuPb SMD mill discharge	Composite 4 samples over 1 hour	Manual
CuPb Combined return to rougher	Composite 4 samples over 1 hour	Manual
Zn scavenger concentrate	Composite 4 samples over 1 hour	Manual
Zn Cleaner 1 tails	Composite 4 samples over 1 hour	Automated
Zn Hydrocyclone feed	Composite 4 samples over 1 hour	Manual
Zn Hydrocyclone overflow	Composite 4 samples over 1 hour	Manual
Zn Hydrocyclone underflow	Composite 4 samples over 1 hour	Manual
Zn SMD mill discharge	Composite 4 samples over 1 hour	Manual

The hand samplers used were stainless steel samplers, selected for the various streams based on the flow and particle size present.

Due to the complexity of the recycle streams it was decided to check the flotation performance of the regrind circuit by using a laboratory flotation test. A test would be conducted on the regrind circuit feed and then a separate flotation test using the same conditions on the combined product from the regrind circuit.

During the survey regrind feed samples from both the CuPb and Zn circuits were collected and tested in the onsite laboratory to determine the effect of the regrind process. Due to sampling issues caused by a difficult pipe discharge location, it was not possible to sample the combined regrind stream return pipe for the zinc regrind circuit. Therefore, it was decided to sample the hydrocyclone overflow and mill discharge streams separately and then recombine in the same ratio as the operation circuit.

2.5 Boliden Garpenberg Sample Testing and Analysis

The combined regrind circuit product, SMD regrind discharge and hydrocyclone overflow, were floated in a laboratory flotation machine. Both tests were conducted in a four-liter flotation cell at the sampled solids concentration.

The CuPb tests were conducted for a period of 3.0 minutes, during this time froth was collected, final froth concentrates and tailings were filtered, dried and assayed. The measured pH was 8.2 and the reagents used were 1 drop of Nasfroth frother and 5 g/mt of potassium amyl xanthate (KAX) for the regrind product samples, a conditioning time of 1 minute was allowed before flotation air was applied.

Separate flotation tests were also conducted on the CuPb regrind mill feed and CuPb regrind mill discharge to further determine the effect of the regrind on the liberation and surface conditioning of the regrind streams.

The CuPb tests were conducted for a period of 4.5 minutes split into 3 equal intervals, a separate froth concentrate sample was collected for each time interval. The measured pH was 8.7 and the reagents used were 1 drop of Nasfroth frother for the regrind feed samples. The pH for the regrind discharge sample was 8.5 and as well as the frother a small dosage of collector, 10 g/mt per interval, was added due to the removal of the collector from the particle surfaces by the milling action.

The Zinc (Zn) tests were conducted for a period of 2.5 minutes, during this time froth was collected, final froth concentrates and tailings were filtered, dried and assayed. The measured pH was 7.7. The sphalerite was activated with 100 g/mt of copper sulphate and conditioned for 1 minute. Flotation reagents used were 1 drop of Nasfroth frother and 5 g/mt of isobutyl xanthate for the regrind product samples, a further conditioning period of 1 minute was allowed before flotation air was applied.

All laboratory flotation sample metal concentrations were measured using XRF analysis. Survey samples were also screened and the individual size intervals weighed and metal concentrations measured using XRF analysis.

2.6 Mineral Liberation Analysis and Simulated Breakage

Samples from both the Northlands audit and the Garpenberg audits were screened, sampled and submitted for QEMSCAN analysis.

The QEMSCAN® 4300 system at the Camborne School of Mines (CSM), University of Exeter, UK, is based on a Zeiss EVO 50 series SEM and consists of four

light element Bruker SDD (Silicon Drift Droplet) Energy Dispersive X-ray Spectrometers (EDS) and an electron backscatter detector. The data are then processed to produce a simplified mineral/phase list using iDiscover software (version 4.2 SR1). Standard operating conditions are 25kV and 5nA beam using a tungsten filament operating under high vacuum conditions.

For the LIMS feed and products Particle Mineral Analysis (PMA) mode was used to examine part of the polished block initially at an X-ray pixel spacing of 1.5 µm. Once the data was collected a particle processor was used to separate touching particles. The accuracy of the liberation data will be dependent on the X-ray pixel spacing. This will be particularly significant for this high-grade magnetite concentrate where average particle liberation of 95% is required. Selection of an X-ray pixel spacing is a compromise between precision of data (reduced pixel spacing gives improved precision) and run time/cost (reduced stepping interval increases run time and increases costs). With particles having a relatively wide particle size distribution it is best to divide the sample into screen fractions and run them separately with varying pixel spacing, with finer particles having reduced pixel spacing. This provides better quality data and ensures that more particles are measured in the coarser sizes, but this does involve overall increased preparation costs and instrument running time.

A possible compromise for samples that are already relatively fine/well classified would be to use QEMSCAN to analyse particles in a single block in discrete size ranges with the X-ray pixel spacing varied with particle size. A minimum number of particles could be set to improve the quality of the data in the coarser size ranges. The

QEMSCAN analysis of the other NRAB samples and also the Boliden Garpenberg samples was repeated using this method (Rollinson et al. 2011).

The generated QEMSCAN images were also used, after colour manipulation, for the simulated breakage and recovery technique.

The Voronoi diagram or tessellation of a set of “sites” or “generators” (points) is a collection of regions that divide up the plane. Each region corresponds to one of the sites or generators, and all points in one region are closer to the corresponding site than to any other site. Where there is not one closest point, there is a boundary (Dobrin 2005).

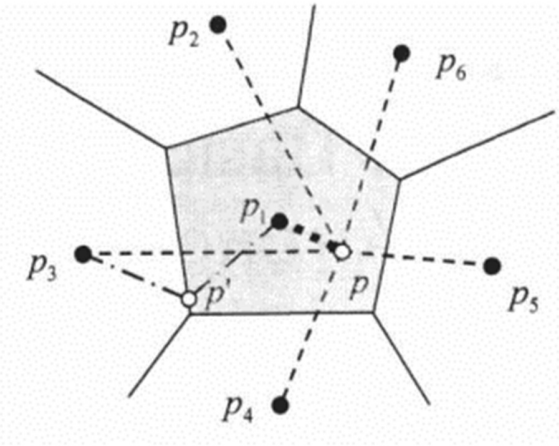

Figure 9 : Fundamental Features of a Voronoi Diagram (Dobrin 2005)

In Figure 9, the point *p* is closer to p_1 than to any other enumerated points, p_2 to p_6. Also note that *p’*, which is on the boundary between p_1 and p_3, is equidistant from both of those points.

Both phases of the liberation simulation were completed in a scientific image analysis program called Fiji. Voronoi tessellations were used as an approximation of a completely random fracture pattern generated during grinding of particles. Voronoi

tessellations are a type of structure used in computational geometry to subdivide a 2-dimensional or 3-dimensional space into many smaller sub-regions or Voronoi cells. A qualitative, visual inspection shows Voronoi cells to resemble typical comminution products: they are irregularly shaped and angular, with a range of shapes from flaky to cubic (van der Wielen and Rollinson 2016).

There is a specific function in Fiji for producing Voronoi tessellations. The density of the tessellation net was varied to provide a size distribution close to the audit mill discharge size distribution, either the Metso Vertimill® or SMD.

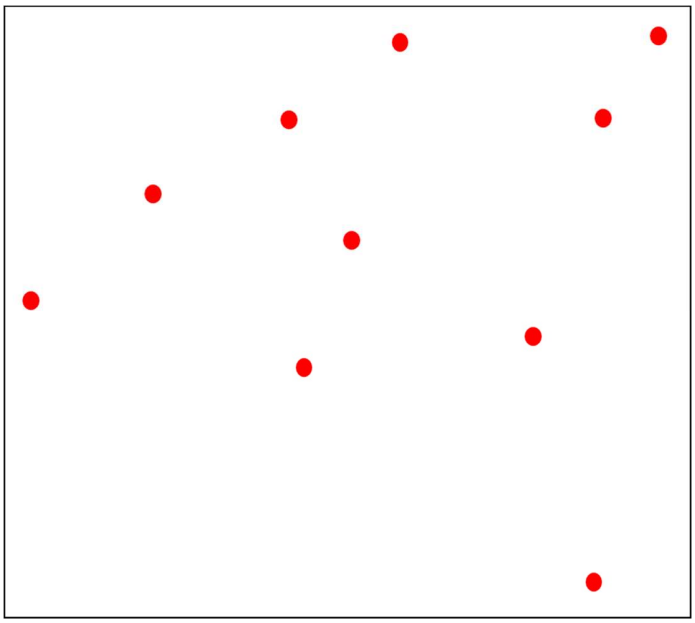

Figure 10 : Generation of random points

Figure 10 shows a random distribution of a pre-specified number of points generated as a seed pattern for the Voronoi tessellation. By increasing the number of points the area of each Voronoi cell is reduced.

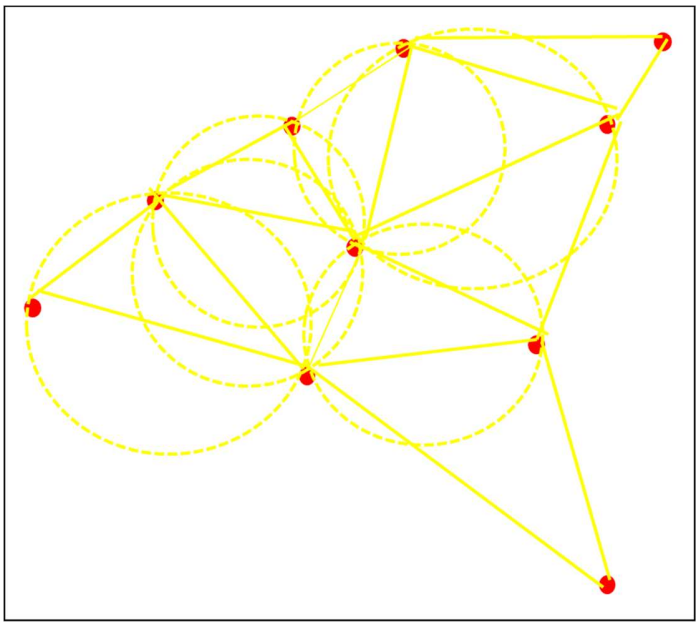

Figure 11 : Random points used to generate Delauney Triangulation

In Figure 11 straight lines join the points (Delauney Triangulation) and the position of the points is used to generate circles. The centers of the circles define the nodes for the Voronoi tessellation (yellow dashed lines).

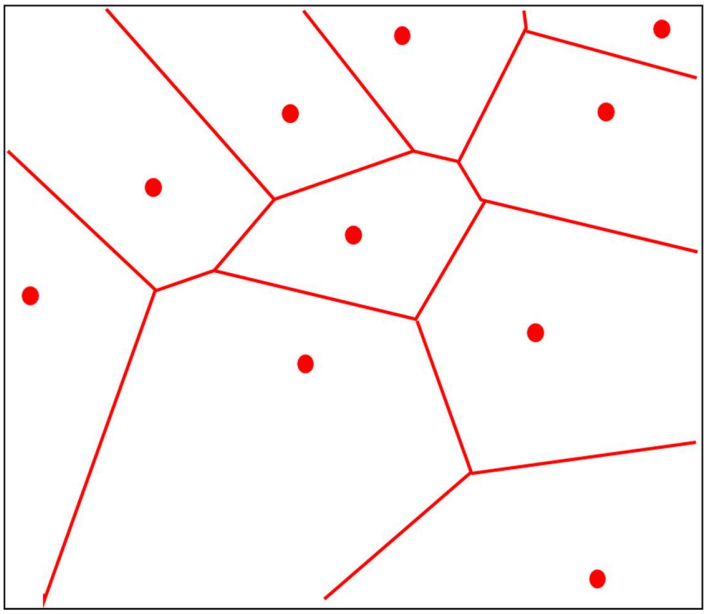

Figure 12 : Voronoi Tessellation Grid Generated

Figure 12 shows the Voronoi tessellation generated from the centers of the circles, with connecting lines running perpendicular to the Delauney Triangulation lines connecting the original points. The tessellation grid or net is now ready to be used for the simulated breakage of the particles.

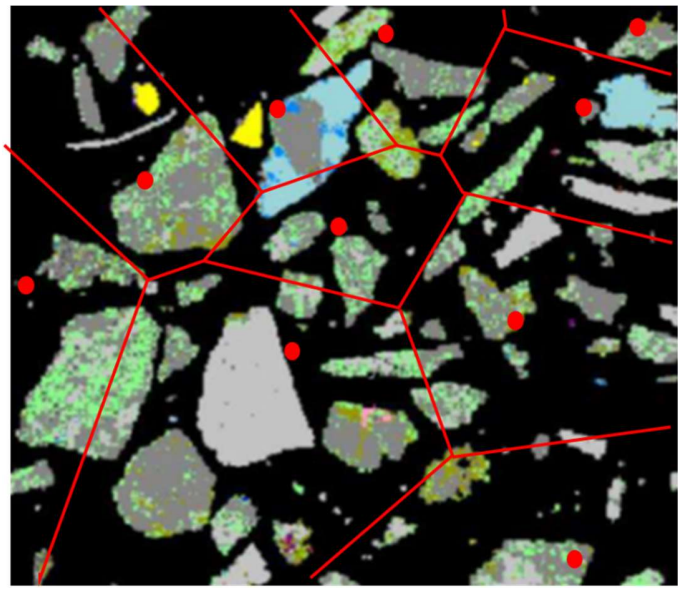

Figure 13 : Tessellation grid overlays the mineral particle digital map

The Voronoi pattern is superimposed on the digital mineral texture in Figure 13, or in this case the mineral particle map, and the mineral map particles are ‘fragmented’ according to the Voronoi tessellation. As stated earlier by increasing the number of random points used to generate the grid the area of the individual cells within the tessellation is reduced, this generates a finer fragmentation or simulated grind size distribution, this is visually shown in Figure 14.

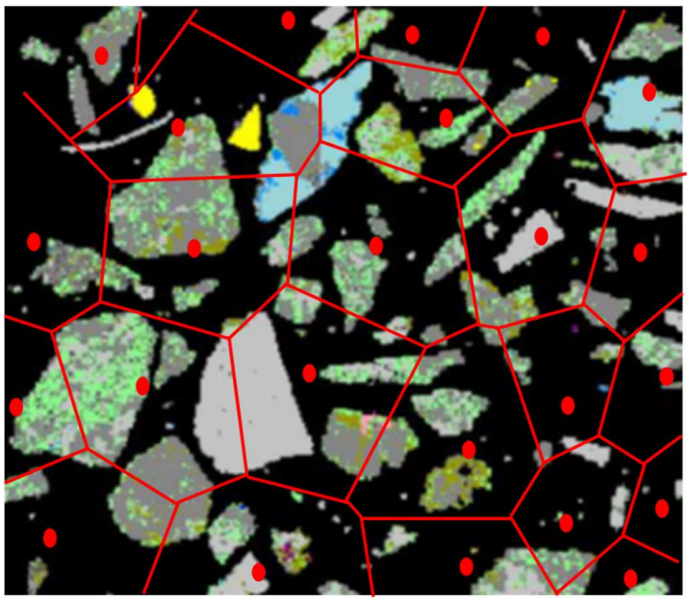

Figure 14 : Diagram showing deduction in grid size by increasing generation points

By increasing the number of random generation points, from 10 to 24, it can be seen by comparing figures 13 and 14 that the grid or net cell size is significantly reduced. This is the method used to generate different particle size distributions.

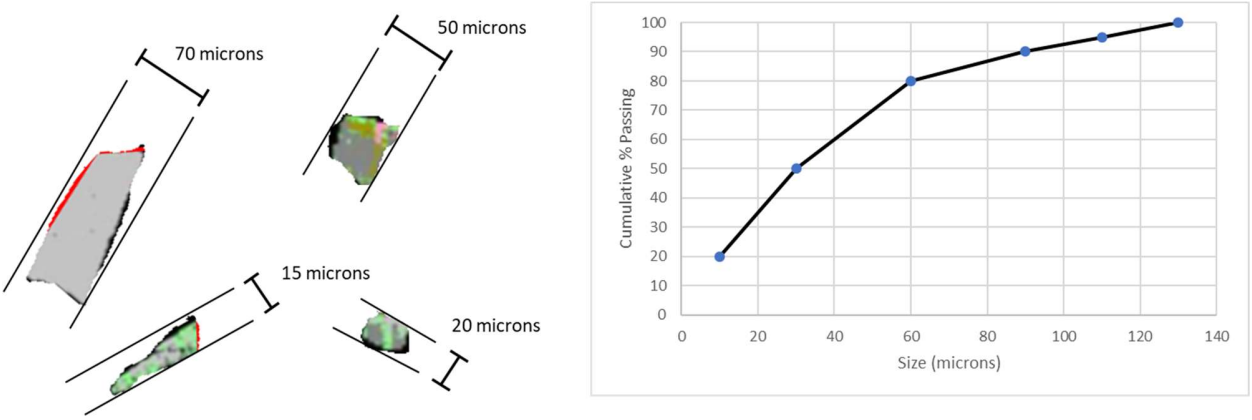

Figure 15 : Feret diameter measurement of simulated fractured particles

Figure 15 shows a visual representation of the fragmented particles. The Feret diameter can be calculated for each particle. The Feret diameters can then be used to

generate a simulated size distribution curve. This process is repeated until a simulated size distribution is generated that has the same 80% passing size as the target size.

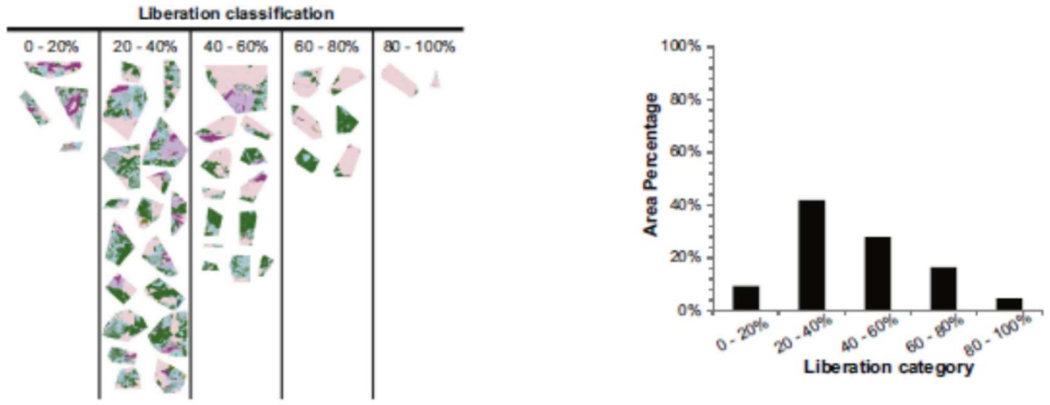

Figure 16 : Mineralogical data captured from the tessellated mineral particle map (van der Wielen and Rollinson 2016)

Each fragmented particle still contains the particle mineralogical data from the QEMSCAN particle map. Therefore, each particles liberation class and data can be generated and presented as shown in Figure 16. The data can also be used for enrichment modelling calculations.

It is possible in Fiji to measure various attributes of a region of interest, including Feret diameter. The Feret diameter defines the distance between two parallel lines tangential to outline of a particle. During screening particles will move around on the screen deck, at some point orienting themselves so that they have the highest probability of fitting through a mesh opening in a screen. In a 2-dimensional representation of the sieving process, this orientation is comparable to the minimum Feret diameter (van der Wielen and Rollinson 2016).

The size data generated and the mineralogical data for the new simulated particles was exported to an excel spreadsheet for further data processing, different

approaches were used for the magnetite sample from Northlands and the sulphide flotation samples from Garpenberg.

For the Northlands sample the data generated from the tessellation work was simulated a Metso Vertimill® discharge product. To simulate the hydrocyclones in the regrind circuit a simple rule of that all particles smaller than 60 microns reported to the hydrocyclone overflow and all particles over 60 microns reported to the underflow, the underflow data was not used for any additional processing.

Each discrete particle was then analysed and the percentage magnetite by mass was calculated. To simulate the LIMS enrichment process all particles with a magnetite content of 5% or less were rejected to a tailings stream or file. The value of 5% was selected based on experience and the magnetic susceptibility of a particle presented in figure 16. Figure 16 plots the magnetic susceptibility against the magnetite content of the particle, K_m/K_0 being the ratio of the mixed particle magnetic susceptibility to the magnetic susceptibility of pure magnetite. It was predicted that particles with a magnetite content of greater than 5% reported to the concentrate stream or file.

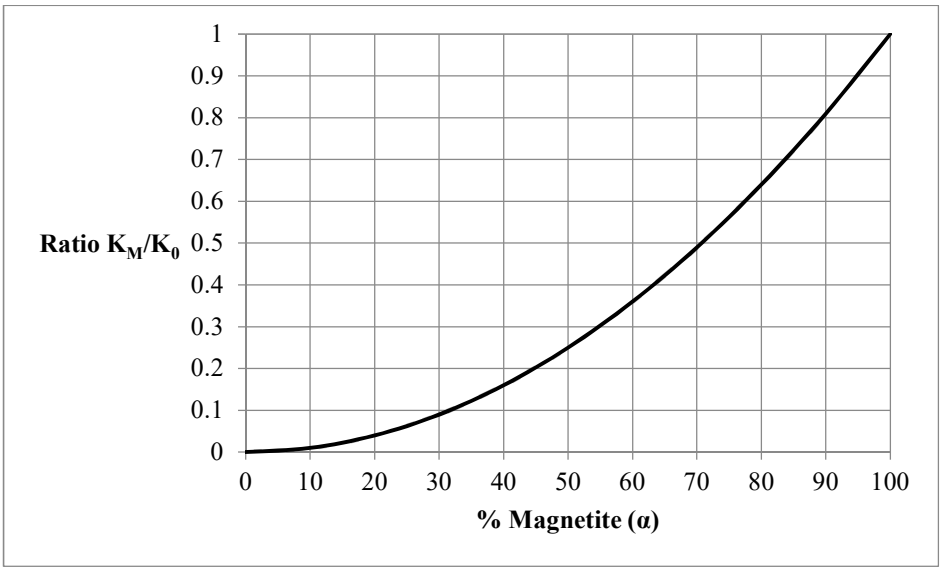

Figure 17 : Ratio of volume magnetite to magnetic susceptibility (Pascoe et al. 2015)

The iron content could then be calculated for both the concentrate and tailings stream, assessing both the iron in the magnetite and any iron in the gangue minerals. The elemental iron content could then be compared to the iron assays measured during the audit and used to calculate an overall recovery.

For the Garpenberg samples analysis and modelling of the tessellation data from the grinding circuit was simpler being an open circuit SMD mill, so the step to replicate the operation of the hydrocyclone was not necessary. For both Boliden Garpenberg samples due to the complexity of the flotation process and the complex mineralogy of the samples it was decided to compare the liberation of the particles from the audit with the simulated SMD product from the tessellation. The liberation of either galena or sphalerite was calculated for each discrete particle from the tessellation data. This data was then sorted and analysed to generate a liberation table with the same liberation classes as the audit SMD mill discharge QEMSCAN data, this could then be compared.

3 Results

3.1 Introduction

The results from the size analysis, metallurgical testing, mineralogical analysis and simulated fracture were assessed using various techniques.

The first stage for the Northlands analysis results was to compare the laboratory metallurgical tests, including mill and enrichment with the results from the concentrator audit. This involved the comparison of size analysis, chemical assay and mineralogical data.

The second stage for the Northlands samples was the simulation of the regrind circuit using the mineralogical map of the feed particles and fracturing the particles using a computer model. The simulated mill product particles could then be magnetically enriched using the mineralogical profile data of the fractured particles and a simple separator model. This was again compared to the values generated from the plant audit.

The Garpenberg audit samples were again compared to the laboratory milling and flotation test samples generated from the laboratory metallurgical tests, involving size analysis, chemical assay and mineralogical data.

The mineralogical map data was then modelled using the same simulated fracture process. Multiple simulations were conducted to assess the impact of the tessellation size and the subsequent liberation of the fractured particles. The size analysis and liberation data for the simulated fractured particles was compared to the audit size data.

3.2 Northlands Survey Results

The size analysis results from the Northlands regrind circuit were mass balanced and plotted.

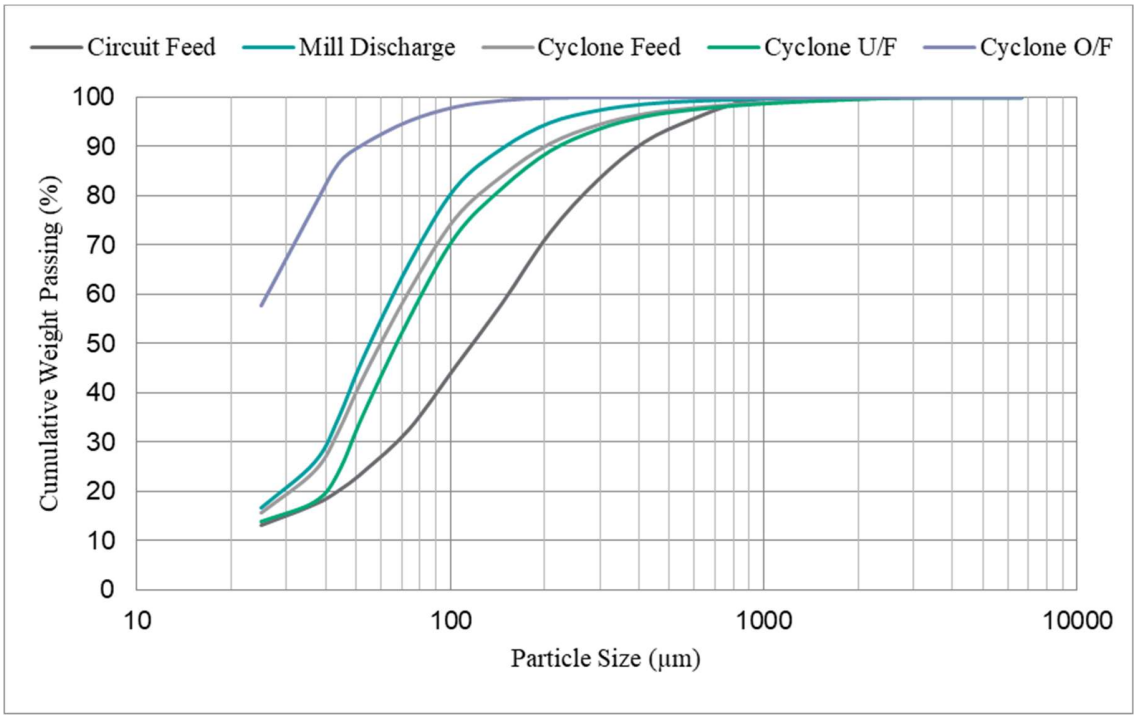

Figure 18 : NRAB Regrind Circuit Audit Size Analysis

The results from the Metso laboratory jar mill test could then be compared to the results from the site audit.

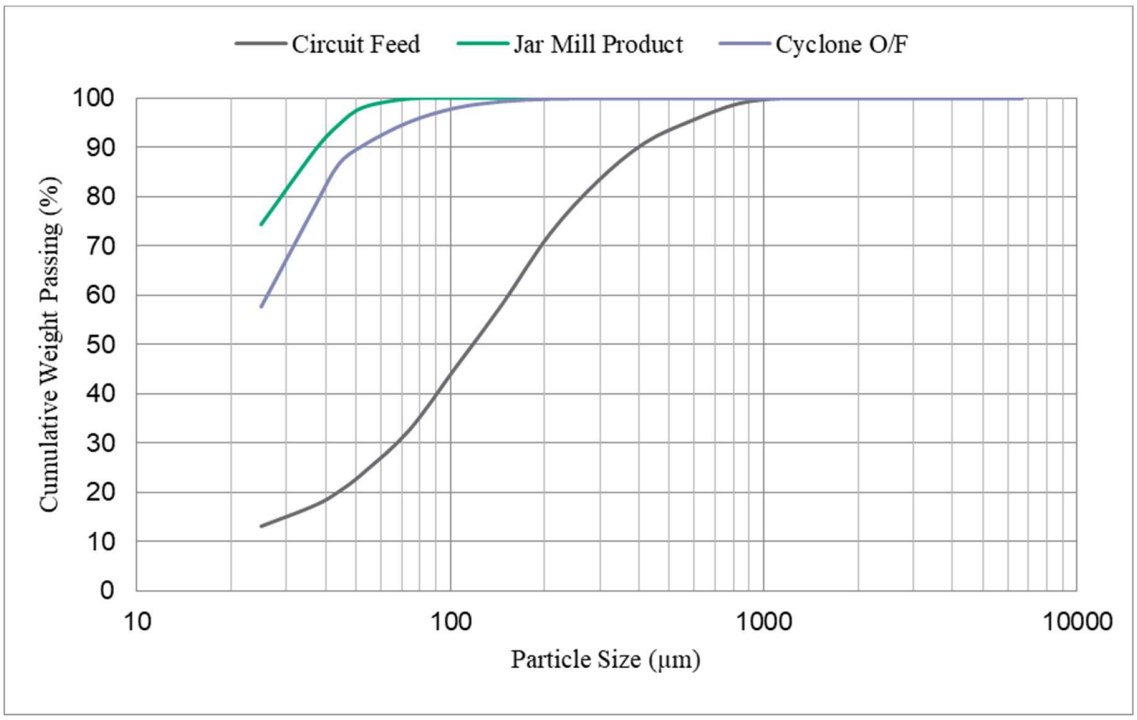

Figure 19 : NRAB Regrind Circuit Audit Size Analysis compared to Metso jar mill data

As can be seen from Figure 19 the jar mill product generated from a 111-minute grind is slightly finer, with an 80% passing size of 29 microns versus 39 microns for the Metso Vertimill® hydrocyclone overflow sample. However, the slope of the two curves is very similar and a slight reduction in the jar mill residence time, to a residence time of 90 minutes, gives a very good correlation between the tests.

The laboratory grinding test showed a good correlation between the jar mill product and the hydrocyclone overflow size distribution as can be seen in Figure 19. Historically laboratory rod mills have been used for sample generation to provide a test sample size distribution similar to real plant conditions. However, as described by Runge often a laboratory ball mill now fits the product distribution from modern plants better than a laboratory rod mill (Runge et al. 2013). With many plants now grinding

significantly finer and by using a mono sized ball charge in the Metso jar mill the resulting size distribution provides a good correlation to the plant audit data.

The divergence in the jar mill size distribution curve and the hydrocyclone overflow size distribution curve above 50 microns is relative small and probably caused by the bimodal size distribution and the density difference between the minerals in the ore affecting the classification process in the hydrocyclone. Although, this difference is small it has a significant knock on effect on the subsequent downstream magnetic enrichment step.

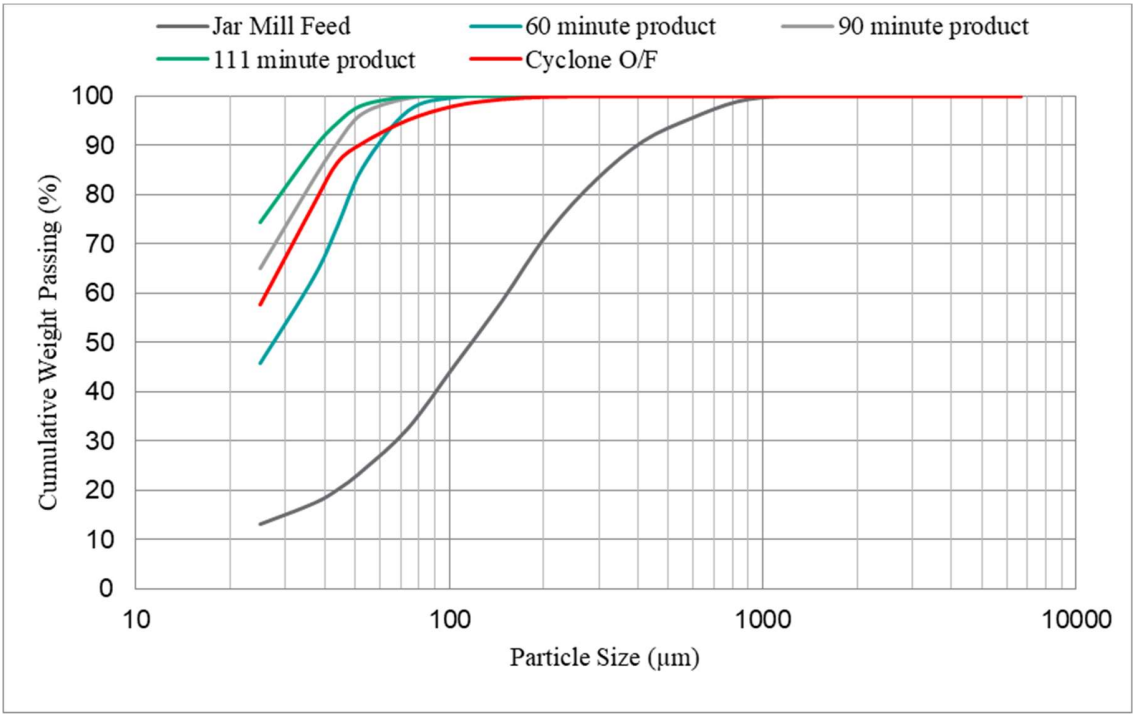

Figure 20 : Full Metso jar mill data for the NRAB Metso Vertimill® fresh feed sample

Although the slope of the lab jar mill and Metso Vertimill® hydrocyclone overflow are similar, above 50 microns the hydrocyclone size distribution slope is flatter than the lab jar mill, this is partly due to the lab jar mill being a batch mill so no bypass of

particles is possible. The slope is also due to the bimodal nature of the hydrocyclone feed slurry especially the density difference between the magnetite particles and the main gangue minerals, such as silicates. This density difference results in a different cut point within the hydrocyclone for the magnetite and the gangue, the magnetite having a finer cut point than the gangue minerals.

This is a major problem in all magnetite processing circuits because the lighter gangue particles may still contain a small quantity magnetite and could report to the final concentrate, reducing the overall iron grade of the concentrate (Pascoe et al. 2015).

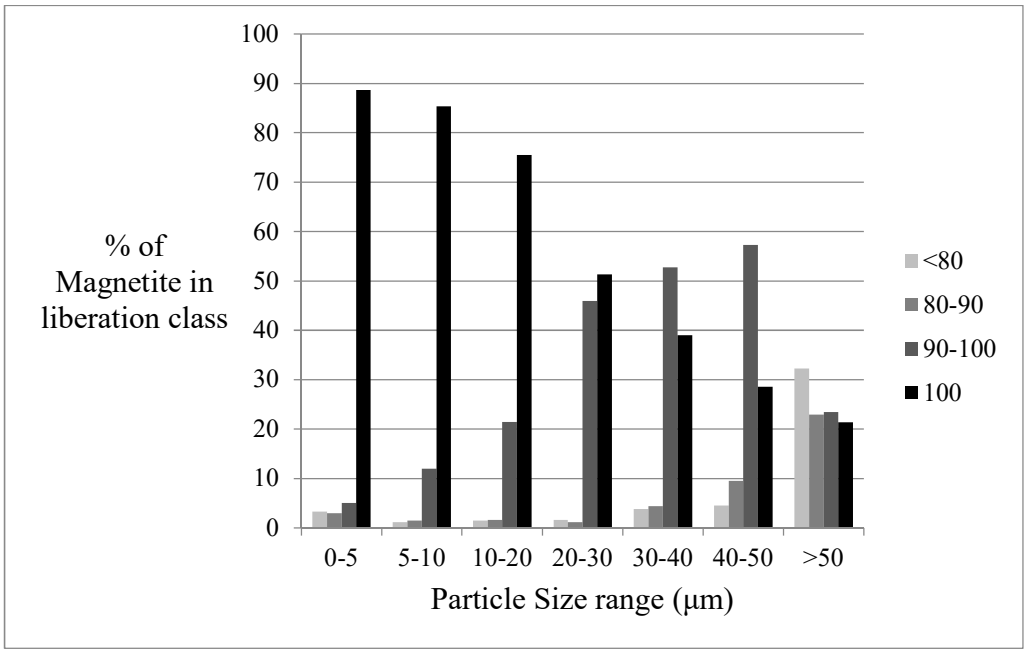

Figure 21 : NRAB QEMSCAN data showing bimodal distribution of magnetite and gangue

A series of Davis tube tests were conduct on the bulk sample collected from the Metso Low Intensity Separators (LIMS) which are the final enrichment stage in the NRAB regrind circuit. The values from the site audit around the LIMS were as follows:

Table 5: NRAB LIMS audit results

	assay / value	
	Fe	SiO_2
LIMS feed	57.8	7.7
LIMS concentrate	69.1	1.61
LIMS tails	5.77	21.6
LIMS recovery	98.2	14.5

The final product from the jar mill test was then processed using a Davis tube separator to determine the effect of the different size distribution, especially for the magnetite and gangue.

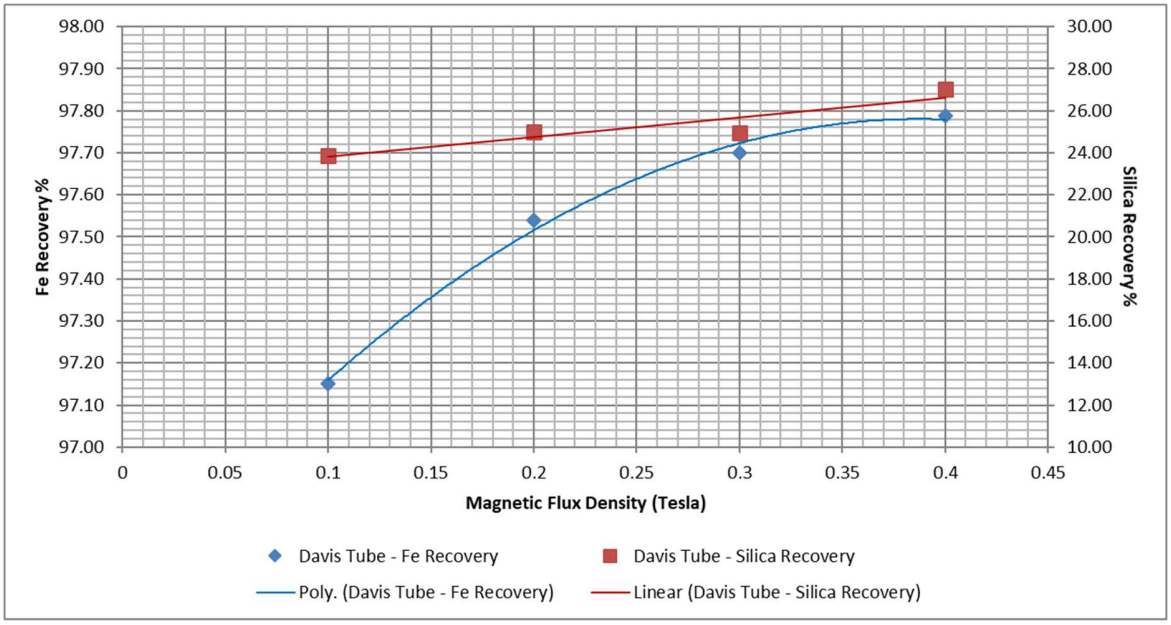

Figure 22 : Davis tube Fe and SiO_2 Recovery at different Magnetic flux densities

Based on the previous work by Murariu (Murariu and Svoboda 2003) it was decided to use the 0.1 Tesla Davis tube results to compare with the results from the LIMS in the NRAB regrind circuit and the Davis tube test conducted on the jar mill product.

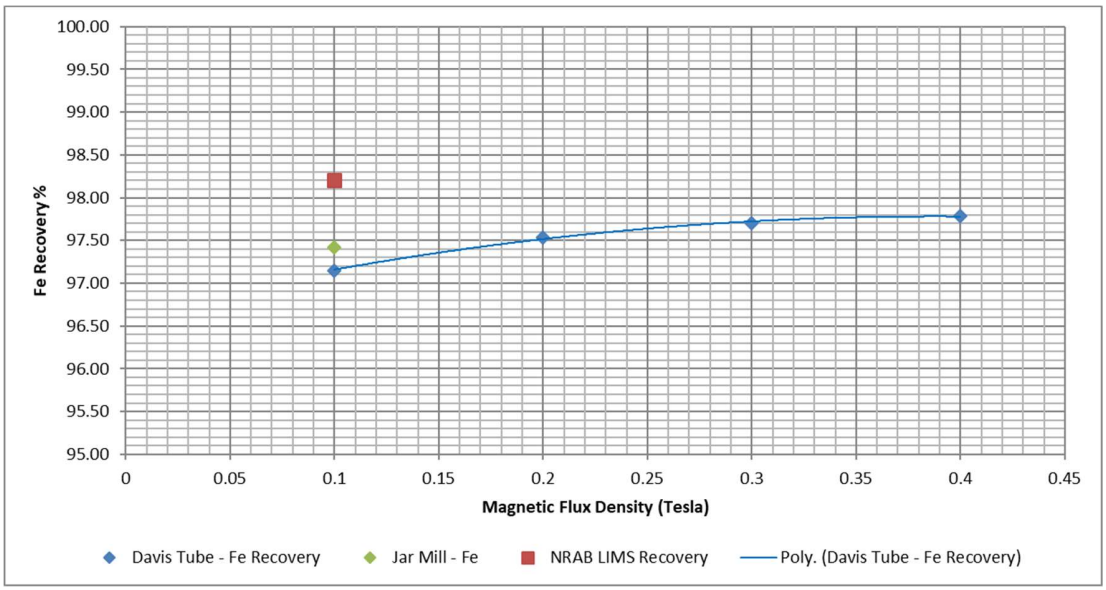

Figure 23 : Fe recovery data from jar mill product Davis tube and LIMS data from audit

As can be seen from Figure 23 the jar mill test recovery and plant LIMS feed recovery are very close. The plant LIMS concentrate is higher, however the LIMS separator consists of three drum stages for additional cleaning of the concentrate. The agitation between the stages and the three stages of enrichment account for the slightly improved recovery.

The Davis tube testwork showed a good correlation between the Northlands concentrator audit LIMS separator sample and the Davis tube concentrate and tailings samples for both the iron assays and iron recovery. The LIMS concentrate grade was 69.1% Fe compared to 67.6% Fe for the Davis tube, the recovery was 98.2% compared to 97.2%. The values for the silica grade and recovery were 2.38% SiO_2 and 23.9%, compared with the plant values of 1.61% SiO_2 and 14.5%. The main issue with the Davis tube test was the single run of the test compared to the 3 drum stages in the Northlands plant LIMS separator. The aim of the three-stage separator is to dilute and agitate the concentrate from the previous stage before further enrichment. This should

have limited effect on the iron recovery, however the multiple stages of cleaning do reduce the entrapment of non-magnetic gangue particles, by agitating and breaking magnetically flocculated clumps of particles.

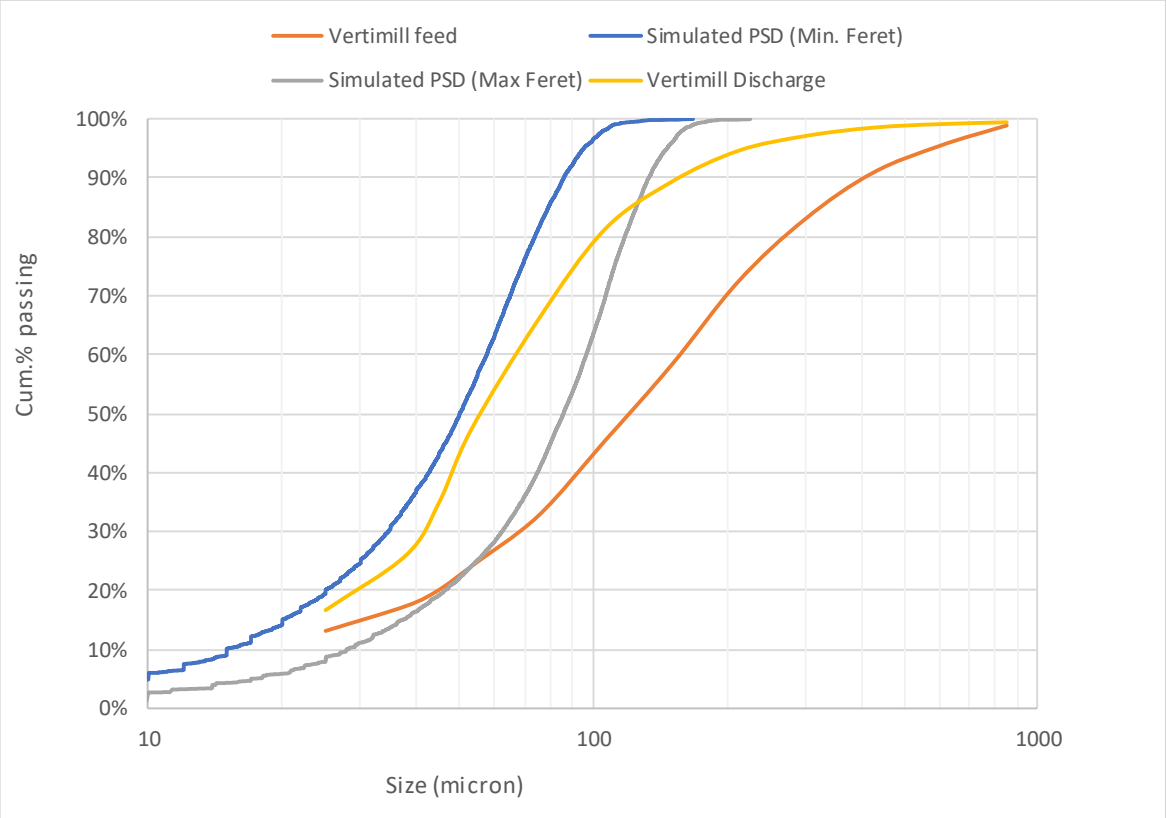

Figure 24 : Particle Size Distribution comparing computer simulated breakage with audit data

Using the computer model generated breakage data, it was possible to generate a breakage product size distribution curve for both the minimum and maximum ferret lengths which is shown in Figure 24. The Feret length is considered the best dimension for comparison to sieve data as generated during the analysis of the NRAB audit data.

As can be seen in Figure 24 the modelled data has a similar slope for both the minimum and maximum ferret length when compared to the audit Metso Vertimill® discharge size distribution below the 80% passing size. However, above the 80% passing size the audit data deviates significantly from the model data. The audit data shows a significant tail to the mill discharge curve possibly due to inefficient grinding on the particles or bypass within the mill. These particles would be classified by the regrind circuit hydrocyclones and returned to the Metso Vertimill® for further grinding.

It may also be that the tessellation grid or model used was too fine resulting in an overly fine product. All mills will have some bypass and a higher grinding mill circulating load improves efficiency (McIvor 2014). a model could be produced that ‘bypasses’ some of the mill feed to the modelled product data combining with the finer tessellation data. By adjusting the ratio of fresh feed or bypass to the ratio of tessellation data it should be possible to produce a modelled curve very close to the audit data size distribution curve.

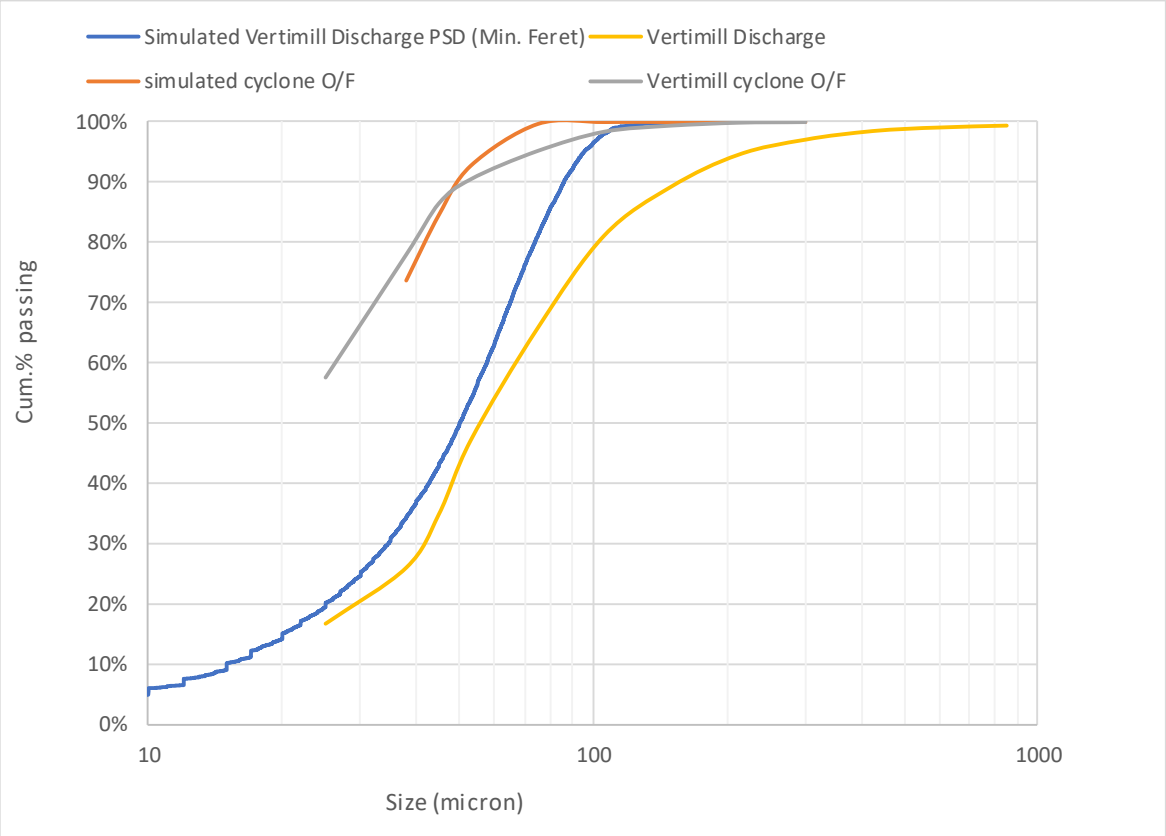

Figure 25 : Particle Size Distribution comparing simulated hydrocyclone overflow with audit data

The simulated Metso Vertimill® discharge data was then modelled using a simple excel hydrocyclone performance spreadsheet to simulate the regrind circuit hydrocyclone overflow size distribution. The comparison shows that the simulated curve has a similar slope and almost identical 80% passing size. However, the curves do diverge in the coarser size fractions, this is to be expected due to the lack of coarser material in the simulated mill discharge data. Also, the differences in the particles densities cause a slightly bimodal affect in the audit data, no attempt was made to compensate for the particle densities in the simulated data, although this would be possible with a more complex model.

Finally, an attempt was made to use the mineralogical data generated from the tessellation breakage data. To simplify the simulation data processing, it was assumed that all particles finer than 60 microns reported to the hydrocyclone overflow and all particles coarser than or equal to 60 microns reported to the hydrocyclone underflow. It was then further assumed that the circuit was in equilibrium so no further data processing of the hydrocyclone underflow data was required.

The hydrocyclone overflow data set, which now consisted only of particles finer than 60 microns was data processed to simulate the effect of the LIMS magnetic separators. The quantity of magnetite in each particle was calculated from the mineralogical data and then all particles with less than 5% magnetite content were calculated to report to the LIMS non-magnetic tailings, all other particles were calculated to have reported to the LIMS magnetic concentrate.

A calculation was then conducted for all particles in both the magnetic concentrate and non-magnetic tailings data sets to calculate the mass and %Fe reporting to the simulated process streams, the simulated and audit data is shown in Table 6.

Table 6: Simulated Regrind Circuit Data compared with Plant XRF data

	Simulated	Actual Plant Audit
LIMS Feed Grade	61.4 %Fe	57.8 %Fe
LIMS Concentrate Grade	70.3 %Fe	69.1 %Fe
LIMS Tailings Grade	8.8 %Fe	5.77 %Fe
LIMS Mass Recovery to Concentrate	85.1%	82.2%
LIMS Fe Recovery to Concentrate	97.9%	98.2%

The results indicate a good simulation of the results, the simulated results for the assay values are even closer to the assay results generated from the QEMSCAN analysis, tabulated in table 7, rather than the XRF results from the audit mass balance.

Table 7: Simulated Regrind Circuit Data compared with QEMSCAN assay data

	Simulated	QEMSCAN data
LIMS Feed Grade	61.4 %Fe	61.8% Fe
LIMS Concentrate Grade	70.3 %Fe	70.2% Fe
LIMS Tailings Grade	8.8 %Fe	7.4 % Fe
LIMS Fe Recovery to Concentrate	97.9%	98.4%

This is to be expected, the QEMSCAN LIMS feed mineralogy being the starting data for the tessellation breakage data processing.

The model used to simulate the downstream hydrocyclone stage and the LIMS magnetic separator was very simple but gave good results. The hydrocyclone model could be improved by using a probability recovery curve to better replicate the probability of a particle reporting to the hydrocyclone underflow or overflow. Also, the tessellation data provides information on the particle mineralogy which could be used to calculate a particle specific gravity. This particle specific gravity data could then be added to the hydrocyclone model to better simulate the probability of low specific gravity particles preferential reporting to the hydrocyclone overflow compared to a high specific gravity particle of the same size.

The main magnetite losses to the LIMS tailings were in the ultrafine particles, which is the normal area of concern for most magnetite operations. However, it was also found that magnetite losses were not as high as expected which is due to the ultrafine particles agglomerating due to magnetic flocculation. The agglomerated groups of particles are then large enough to overcome the hydrodynamic forces within the

magnetic separator and attach to the magnetic drum, thus reporting to the magnetic concentrate.

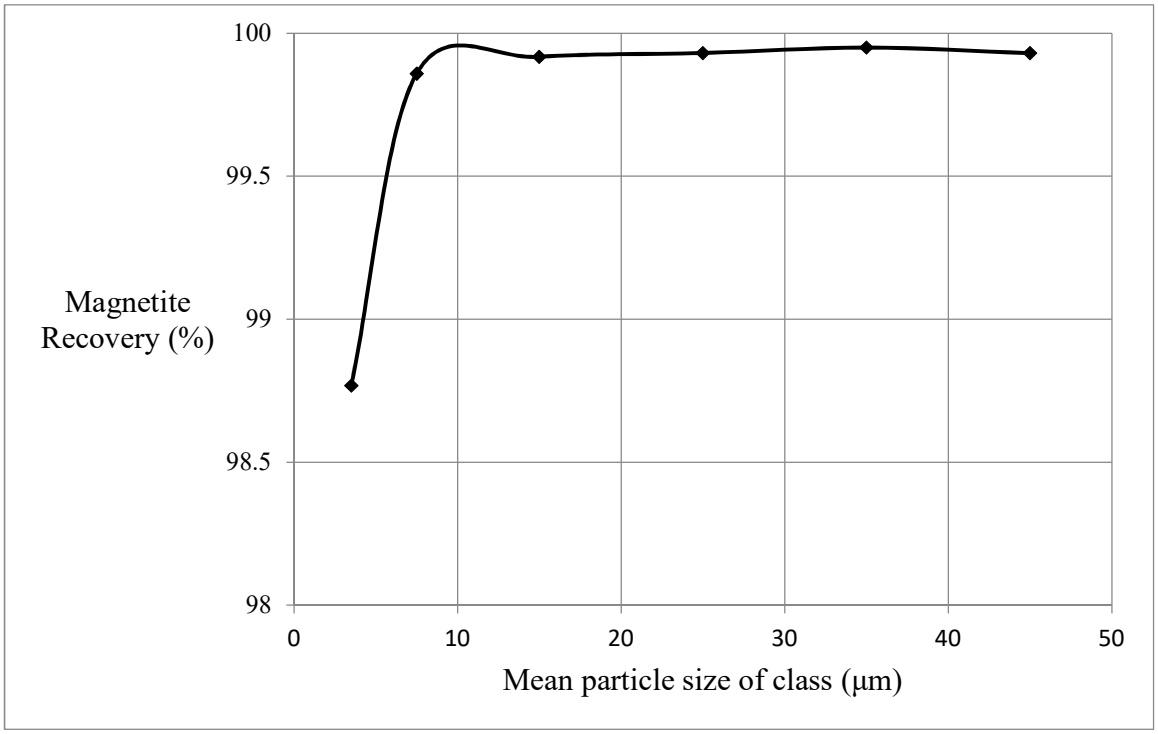

Figure 26 : Northlands LIMS Magnetite Recovery

The negative consequence of this magnetic agglomeration is that the ultrafine magnetite agglomerates have sufficient strength to bind or trap non-magnetic particles within the agglomerates. This gives rise to losses as both entrainment or entrapment and poor liberation in the plus 45-micron size classes.

Traditionally, the final stage of LIMS separation contains multiple stages with water addition to agitate and break any magnetic agglomerates. However, by analysing the QEMSCAN data in Figure 26 it was found that the turbulence or mixing generated by the multiple drum LIMS separators at Northlands is insufficient to break the agglomerates allowing ultrafine gangue to report to the magnetic concentrate. The amount of contamination is low due to the low level of gangue in the feed, however

Figure 27 shows 37% of the 2-5 micron particle size range reported to the magnetic concentrate due to entrainment in magnetic agglomerates. Parian et al. showed that entrapped fine particles typically drain through the coarser particles. With the very fine grind conducted at Northlands this would not be possible, the magnetite agglomerate particles are as small or smaller than the gangue so limited drainage is possible and entrapment of the gangue continues, this contaminating the magnetic concentrate.

In flotation cells, it has been determined through analysis of laboratory and industrial cells that little entrainment occurs with particles above 50 microns, however at a particle size of 5 microns entrainment is almost 100%. Drawing an analogy between magnetic separation entrapment and entrainment in a flotation cell froth, the risk of gangue particle entrapment will increase in magnetic enrichment processes with finer grinding of the iron ore.

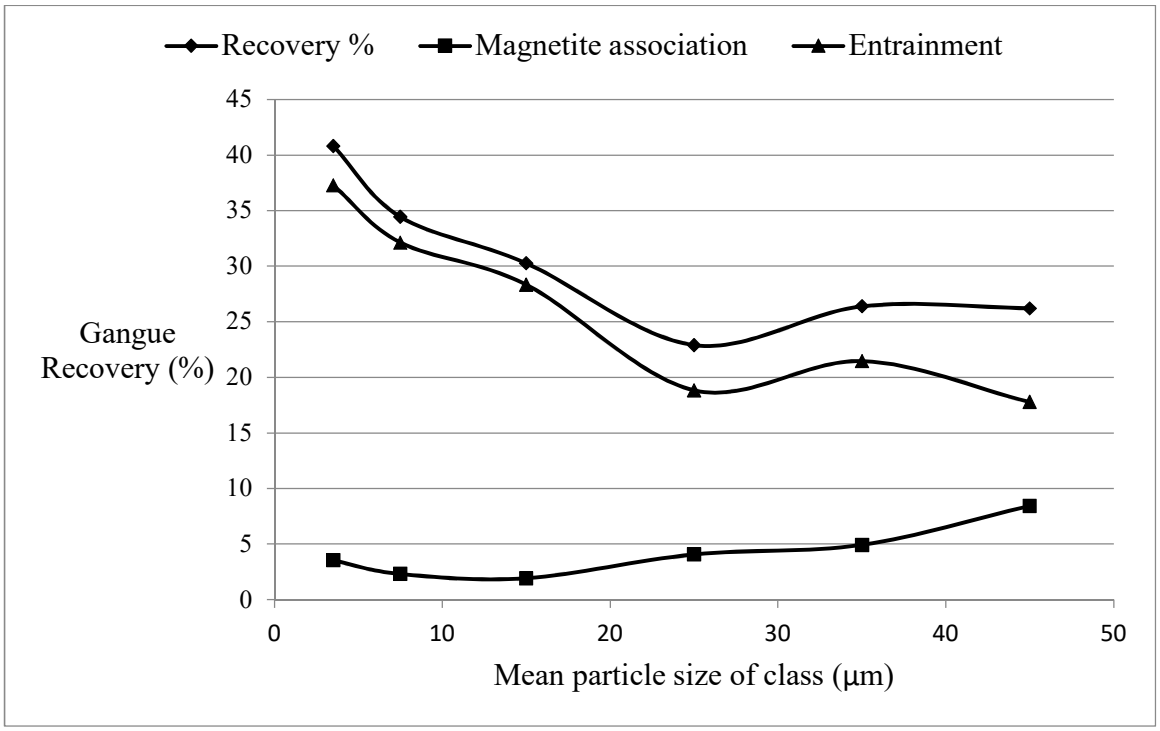

Figure 27 : Northlands LIMS Gangue Recovery (Pascoe et al. 2015)

As can be seen in Figure 27 at the coarse end of the gangue recovery curve the proportion of recovery from entrainment / entrapment and magnetite association, or lack of liberation, is approximately 70% entrainment and 30% magnetite association. At the fine end of the recovery curve around 90% of the gangue recovery to the concentrate is due to entrainment or entrapment.

The combined Metso jar mill followed by a Davis tube, which represents the likely procedure for a green field site, gave results which were very close to the plant audit values. The values for the iron grade and recovery were 69.6% Fe and 97.4%, compared with the plant values of 69.1% Fe and 98.2%. The values for the silica grade and recovery were 1.21% SiO_2 and 13.8%, compared with the plant values of 1.61% SiO_2 and 14.5%. This initial appears to be an excellent result and a confirmation of the jar mill and Davis tube procedure. However, from the Davis tube work conducted on the

audit sample for the LIMS feed it was determined that the Davis tube gave good correlation for the iron recovery but only average correlation for the iron grade, due to the single stage and lack of cleaning in the Davis tube test. Therefore, it is necessary to examine the jar mill – Davis tube combination test more closely to determine the reason for the result.

From the size distribution data, it was determined that although the slope of the jar mill curve gave a good correlation to the hydrocyclone overflow size distribution curve the section above 50 microns showed a marked deviation. As already discussed this is due to the batch nature of the jar mill and differential classification of different minerals within the hydrocyclone. This affects the performance of the enrichment process within the Davis tube, coarse low-density gangue particles, often containing a small amount of locked magnetite, are ground in the jar mill and can then be separated by the Davis tube, reducing the amount of coarse gangue in the final concentrate. This also gives a slight boost to the iron recovery.

The Davis tube test is a relatively old test and limited modifications, if any, have been made to the test equipment or procedures. To improve the washing and agitation of the bed contained by the magnet during operation it would be possible to use wash water to flush the bed. With a modern low flow digitally controlled peristaltic pump it would be possible to flush the magnetite-gangue zone during operation, the amount of flush water could be varied to match the operation of the full size LIMS separators. Some operators (Dworzanowski 2012) have conducted a cleaning Davis tube test on the product from the first stage or roughing test, however due to the small quantities of

sample used during the roughing stage this is a complicated and time consuming procedure.

A more detailed survey of the three stage LIMS separator, including QEMSCAN analysis, with collection of concentrate and tailings from the separate drums would provide useful information of the stage recovery and gangue rejection. Sampling the intermediate drums is a complex procedure, however the benefits in improved separator design to reduce gangue entrapment due to magnetic flocculation would warrant the extra effort.

3.3 Boliden Garpenberg Survey Results

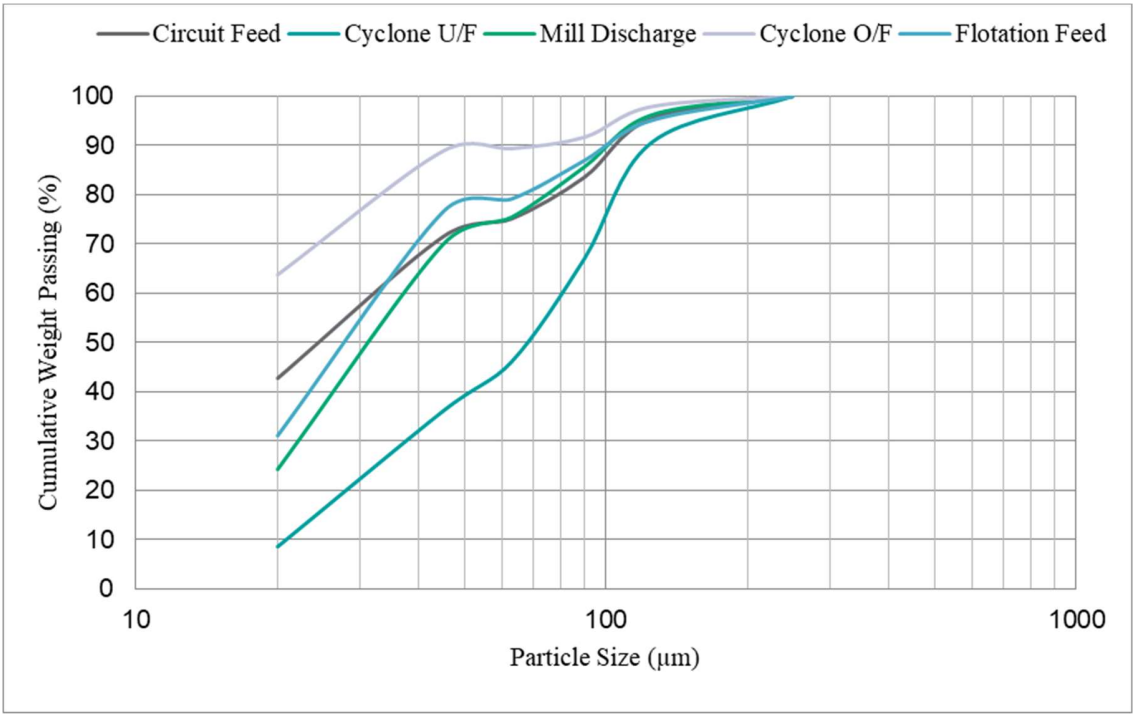

Figure 28: Garpenberg CuPb Regrind Audit Size Distributions

As can be seen in Figure 28, which plots the audit data, the degree of size reduction is relatively small for the CuPb regrind SMD, this is partly due to plant limitations caused by hydrocyclone array feed pump running at too low a speed. The

speed cannot currently be increased due to limits with the pump motor power. Currently this has a low priority due to the good flotation results obtained with the current regrind circuit product.

The reason for the slight step in the size distribution curves at around 45 microns is due to a change in the size analysis method. This applies to all size analysis data generated from Garpenberg.

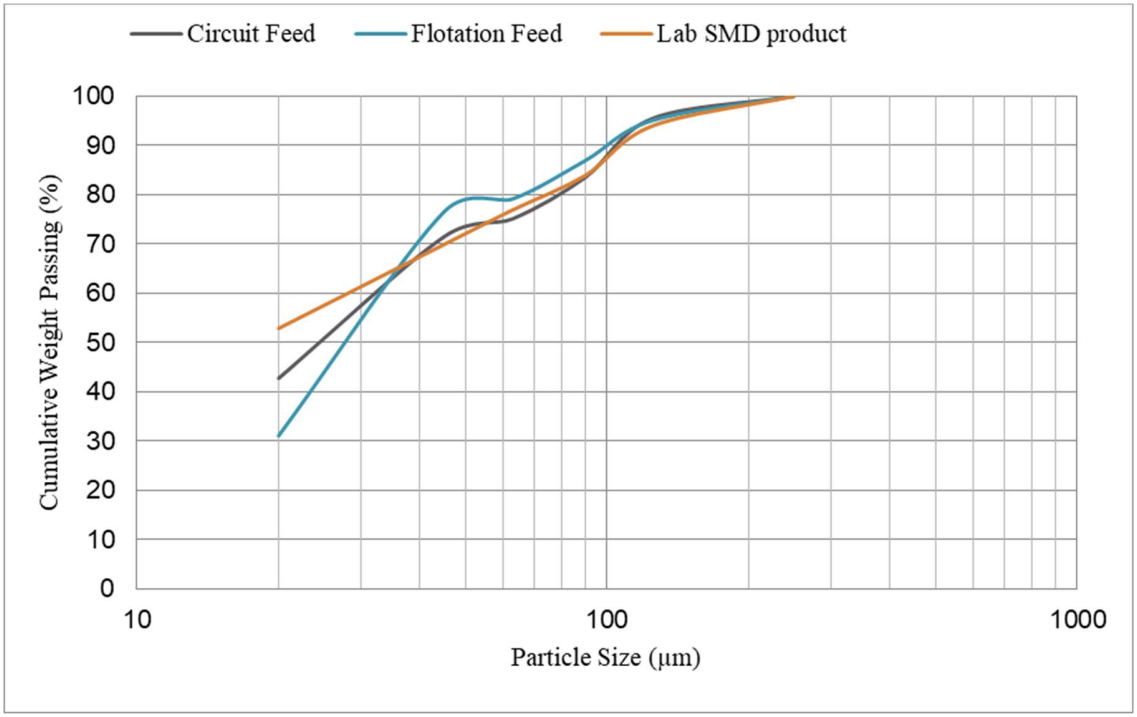

Figure 29 : Comparison between the CuPb regrind circuit product and a lab SMD test on a similar Pb regrind sample from another project

The lab SMD curve has a similar top size but the slope diverges from audit data, ideally a lab SMD test would have been conducted on the Garpenberg feed sample, however the sample was lost in transit.

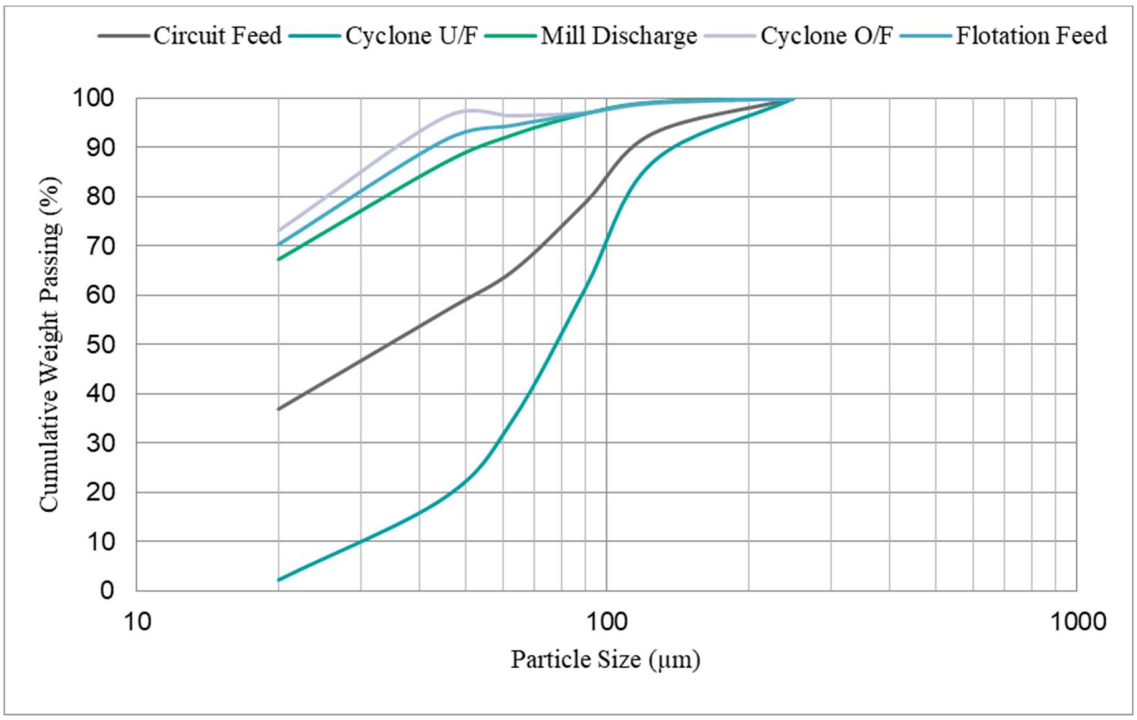

Figure 30 : Garpenberg Zn Regrind Circuit Audit Size Distributions

The audit values for the zinc regrind circuit show a significant size reduction, from a feed of 80% passing 90 microns to an SMD discharge of 80% passing 32 microns. When recombined with the hydrocyclone overflow this results in a flotation feed size of 80% passing 29 microns.

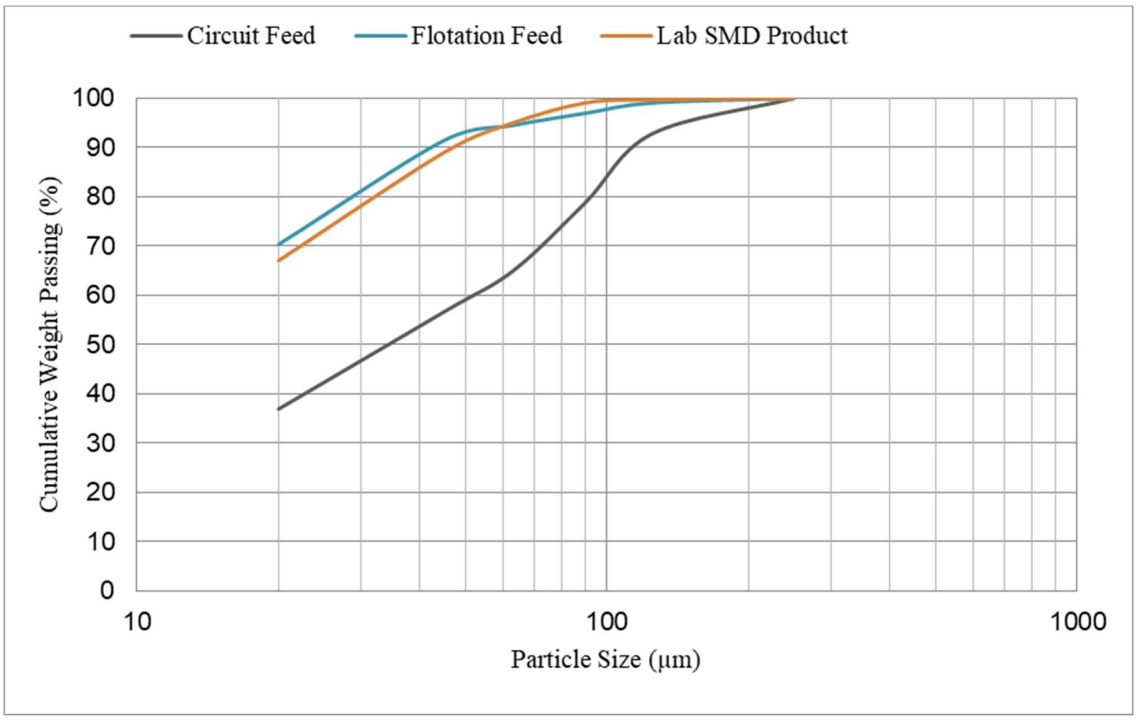

Figure 31: Comparison between the Zn regrind circuit product and a lab SMD test on a similar Zn regrind sample from another project

The indicative laboratory SMD curve from historical data provides a good correlation to the zinc regrind flotation product size distribution. This indicates that a batch laboratory SMD test would provide a suitable product for subsequent or downstream enrichment tests, such as flotation or magnetic separation.

The laboratory SMD tests correlated well with the zinc audit data, but less well with the CuPb audit with a deviation in the product size distribution curve slope at the finer end of the curve. The reduction ratio in the CuPb regrind circuit was very low, 1.05, which can be difficult to replicate in a laboratory SMD test due to the short residence time. The good correlation between the zinc regrind audit data and the laboratory SMD test indicates that this would be a good method to generate flotation samples for further testing, either using conventional laboratory flotation tests or micro flotation testing. The

reasons for the better correlation on the zinc regrind circuit compared to the CuPb regrind circuit are the finer grind, which is easier to replicate in the laboratory SMD.

Table 8: CuPb Flotation Test 1 Results

Product	Mass	Mass dist.	Cu grade	Cu units	Cu dist.	Pb grade	Pb Units	Pb dist.	Zn grade	Zn Units	Zn dist.	Ag grade	Ag Units	Ag dist.	S grade	S Units	S dist.
	g	%	%	g	%	%	g	%	%	g	%	ppm	g	%	%	g	%
Conc.	300.4	59.3	0.43	1.30	90.4	19.6	58.88	88.8	15.68	47.10	56.4	1200	3604.80	88.2	13.9	41.76	57.7
Tails	206.5	40.7	0.07	0.14	9.61	3.58	7.39	11.2	17.60	36.34	43.6	233	481.15	11.8	14.8	30.56	42.3
Feed	506.9	100.0	0.28	1.44	100.0	13.07	66.27	100.0	16.46	83.45	100.0	806	4085.95	100.0	14.3	72.32	100.0

Table 9: CuPb Flotation Test 2 Results

Product	Mass	Mass dist.	Cu grade	Cu units	Cu dist.	Pb grade	Pb Units	Pb dist.	Zn grade	Zn Units	Zn dist.	Ag grade	Ag Units	Ag dist.	S grade	S Units	S dist.
	g	%	%	g	%	%	g	%	%	g	%	ppm	g	%	%	g	%
Conc.	288.1	56.2	0.42	1.21	89.1	20.2	58.11	87.7	16.4	47.13	54.5	1154	3324.67	86.0	14.0	40.33	54.7
Tailing	224.3	43.8	0.07	0.15	10.9	3.62	8.12	12.3	17.6	39.36	45.5	242	542.81	14.0	14.9	33.42	45.3
Feed	512.4	100.0	0.26	1.36	100.0	12.93	66.23	100.0	16.88	86.50	100.0	755	3867.48	100.0	14.4	73.75	100.0

Table 10: Zn Flotation Test 1 Results

Product	Mass	Mass dist.	Cu grade	Cu units	Cu dist.	Pb grade	Pb Units	Pb dist.	Zn grade	Zn Units	Zn dist.	Ag grade	Ag Units	Ag dist.	S grade	S Units	S dist.
	g	%	%	g	%	%	g	%	%	g	%	ppm	g	%	%	g	%
Conc.	50.1	11.0	0.20	0.10	16.3	2.3	1.14	22.7	42.4	21.26	13.0	149	74.65	18.5	28.9	14.48	10.8
Tailing	405.2	89.0	0.13	0.51	83.73	0.95	3.87	77.3	35.1	142.23	87.0	81	329.43	81.5	29.5	119.53	89.2
Feed	455.3	100.0	0.13	0.61	100.0	1.10	5.00	100.0	35.91	163.48	100.0	89	404.08	100.0	29.4	134.01	100.0

Table 11: Zn Flotation Test 2 Results

Product	Mass	Mass dist.	Cu grade	Cu units	Cu dist.	Pb grade	Pb Units	Pb dist.	Zn grade	Zn Units	Zn dist.	Ag grade	Ag Units	Ag dist.	S grade	S Units	S dist.
	g	%	%	g	%	%	g	%	%	g	%	ppm	g	%	%	g	%
Conc.	50.2	10.8	0.19	0.10	15.3	2.3	1.14	22.5	42.5	21.34	13.0	147	73.79	18.0	28.8	14.46	10.6
Tailing	412.7	89.2	0.13	0.53	84.7	0.96	3.95	77.5	34.7	143.21	87.0	82	336.35	82.0	29.4	121.33	89.4
Feed	462.9	100.0	0.13	0.62	100.0	1.10	5.10	100.0	35.55	164.55	100.0	89	410.14	100.0	29.3	135.79	100.0

Table 12 : Garpenberg CuPb SMD Feed Flotation Assays

Product	mass	mass	Ag	Cu	Pb	Zn	S	Sb	MgO	SiO_2
units	g	%	g/t	%	%	%	%	%	%	%
Feed	1243.1	100	604	0.26	9.39	23.81	23.88	0.062	5.30	20.08
Conc 1-3	437.4	35.2	867	0.52	10.94	19.23	23.01	0.069	10.37	25.65
Conc 1-2	311.8	25.1	899	0.56	12.05	19.04	23.96	0.070	10.84	26.55
conc 1	144.6	11.6	973	0.65	13.74	19.39	29.68	0.075	10.34	29.35
conc 2	167.2	13.5	835	0.49	10.60	18.74	19.01	0.066	11.27	24.13
conc 3	125.6	10.1	789	0.42	8.17	19.70	20.64	0.065	9.21	23.43
Tail 1	1098.5	88.4	556	0.21	8.82	24.39	23.11	0.061	4.63	18.86
Tail 2	931.3	74.9	506	0.16	8.50	25.40	23.85	0.060	3.44	17.91
Tail 3	805.7	64.8	462	0.12	8.55	26.29	24.35	0.059	2.54	17.05

Table 13 : Garpenberg CuPb SMD Feed Flotation Distributions

Product		mass	Ag	Cu	Pb	Zn	S	Sb	MgO	SiO_2
units		%	g/t	%	%	%	%	%	%	%
Feed		100	100	100	100	100	100	100	100	100
Conc 1-3		35.2	50.5	70.6	41.0	28.4	33.9	38.7	68.9	45.0
Conc 1-2		25.1	37.3	54.1	32.2	20.1	25.2	28.2	51.3	33.2
conc 1		11.6	18.7	28.9	17.0	9.5	14.5	14.0	22.7	17.0
conc 2		13.5	18.6	25.3	15.2	10.6	10.7	14.1	28.6	16.2
conc 3		10.1	13.2	16.5	8.8	8.4	8.7	10.5	17.6	11.8
Tail 1		88.4	81.3	71.1	83.0	90.5	85.5	86.0	77.3	83.0
Tail 2		74.9	62.7	45.9	67.8	79.9	74.8	71.8	48.7	66.8
Tail 3		64.8	49.5	29.4	59.0	71.6	66.1	61.3	31.1	55.0

The aim of the CuPb regrind stage is to increase the grade and recovery of the lead, copper and silver, whilst reducing the grade and recovery of the zinc. This has two benefits the lead and copper concentrate grade and recovery is improved and the zinc will report to the following zinc flotation, improving the zinc grade to the zinc flotation stage.

Without the regrind stage, flotation test conducted on flotation feed, the lead and silver grades were 12.1% Pb and 899 g/mt Ag with respective recoveries of 32.2% and 37.3%. The zinc grade in the copper-lead concentrate was 19.0% Zn with a recovery of

20.1%, this resulted in a copper-lead tailing, reporting to zinc flotation, of 25.4% Zn with a recovery of 79.9%.

Table 14 : Garpenberg CuPb SMD Mill Discharge Flotation Assays

Product	mass	mass	Ag	Cu	Pb	Zn	S	Sb	MgO	SiO_2
units	g	%	g/t	%	%	%	%	%	%	%
Feed	664.5	100	598	0.22	9.12	23.41	23.74	0.061	4.81	18.68
Conc 1-3	210.7	31.7	1217	0.55	23.04	18.66	19.51	0.103	7.77	16.59
Conc 1-2	108.5	16.3	1716	0.76	29.90	14.69	16.29	0.131	9.43	18.78
conc 1	48.8	7.3	2563	1.07	27.00	11.46	13.14	0.161	12.74	25.29
conc 2	59.7	9.0	1024	0.50	32.28	17.33	18.86	0.107	6.72	13.46
conc 3	102.2	15.4	687	0.33	15.75	22.87	22.94	0.073	6.01	14.27
Tail 1	615.7	92.7	442	0.15	7.71	24.36	24.58	0.053	4.18	18.16
Tail 2	556	83.7	380	0.11	5.07	25.12	25.19	0.048	3.90	18.66
Tail 3	453.8	68.3	311	0.06	2.66	25.62	25.70	0.042	3.43	19.65

Table 15 : Garpenberg CuPb SMD Mill Discharge Flotation Distributions

Product		mass	Ag	Cu	Pb	Zn	S	Sb	MgO	SiO_2
units		%	g/t	%	%	%	%	%	%	%
Feed		100	100	100	100	100	100	100	100	100
Conc 1-3		31.7	64.5	80.0	80.1	25.3	26.1	53.1	51.3	28.2
Conc 1-2		16.3	46.8	56.7	53.5	10.2	11.2	34.9	32.0	16.4
conc 1		7.3	31.5	36.0	21.7	3.6	4.1	19.3	19.5	9.9
conc 2		9.0	15.4	20.6	31.8	6.6	7.1	15.6	12.6	6.5
conc 3		15.4	17.7	23.4	26.6	15.0	14.9	18.2	19.2	11.7
Tail 1		92.7	68.5	64.0	78.3	96.4	95.9	80.7	80.5	90.1
Tail 2		83.7	53.2	43.3	46.5	89.8	88.8	65.1	68.0	83.6
Tail 3		68.3	35.5	20.0	19.9	74.7	73.9	46.9	48.7	71.8

After the regrind stage, flotation test conducted on SMD mill discharge, the lead and silver grades were 29.9% Pb and 1716 g/mt Ag with respective recoveries of 53.5% and 46.8%. The zinc grade in the copper-lead concentrate was 14.7% Zn with a recovery of 10.2%, this resulted in a copper-lead tailing, reporting to zinc flotation, of 25.1% Zn with a recovery of 89.8%.

Overall, the flotation of the mill feed and product indicated an increase in the lead grade of 17.8% Pb and an increase in the silver grade of 817 g/t Ag. Recoveries also

increased by 21.2% for the lead and 9.5% for the silver. The zinc grade in the tailings remained around the same, however the zinc recovery to the tailings increased by 9.9%.

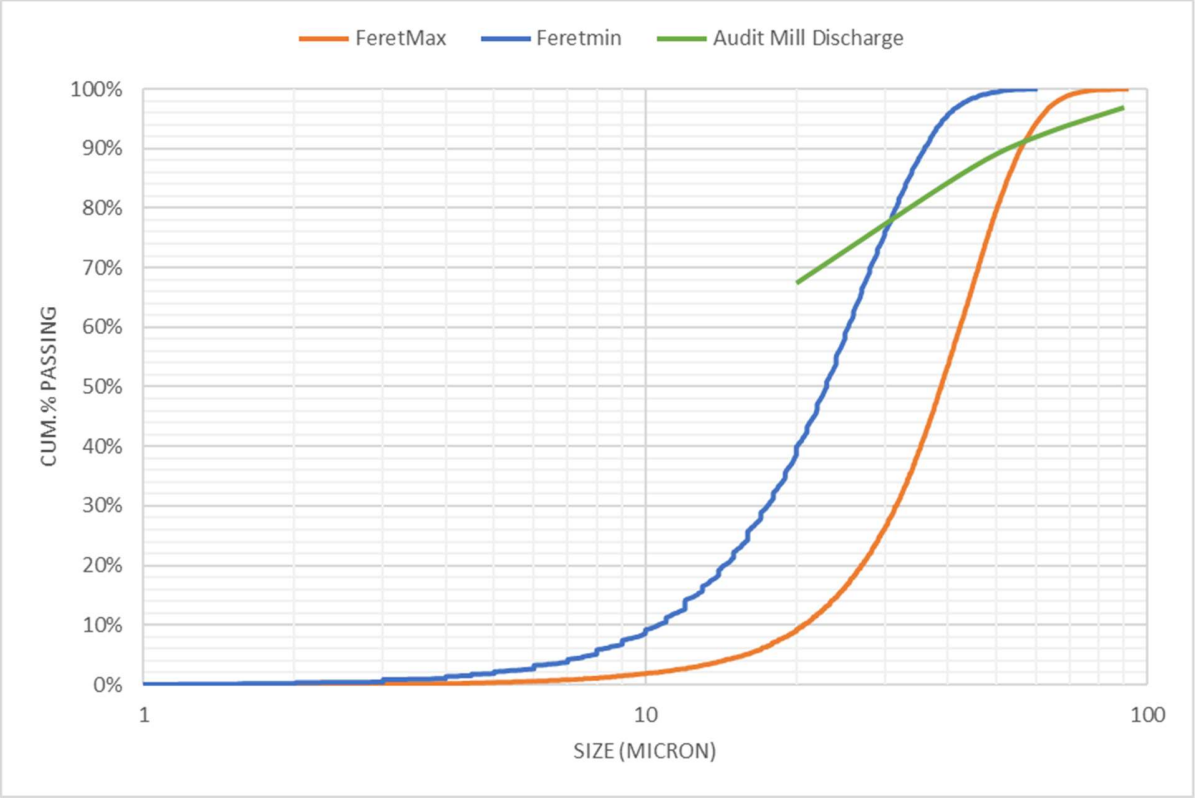

Figure 32 : Boliden Garpenberg Zinc Regrind Mill Discharge Audit and Tessellation Breakage size distribution comparison

The tessellation breakage data for the zinc regrind circuit shows differences in both the particle top size and the slope of the curve, compared to the regrind audit data. The slope of the audit SMD discharge is quite shallow, which may indicate that the media size distribution is quite wide. However, the slope of the tessellation breakage data is certainly too steep, so a poor correlation is obtained between the audit and tessellation data.

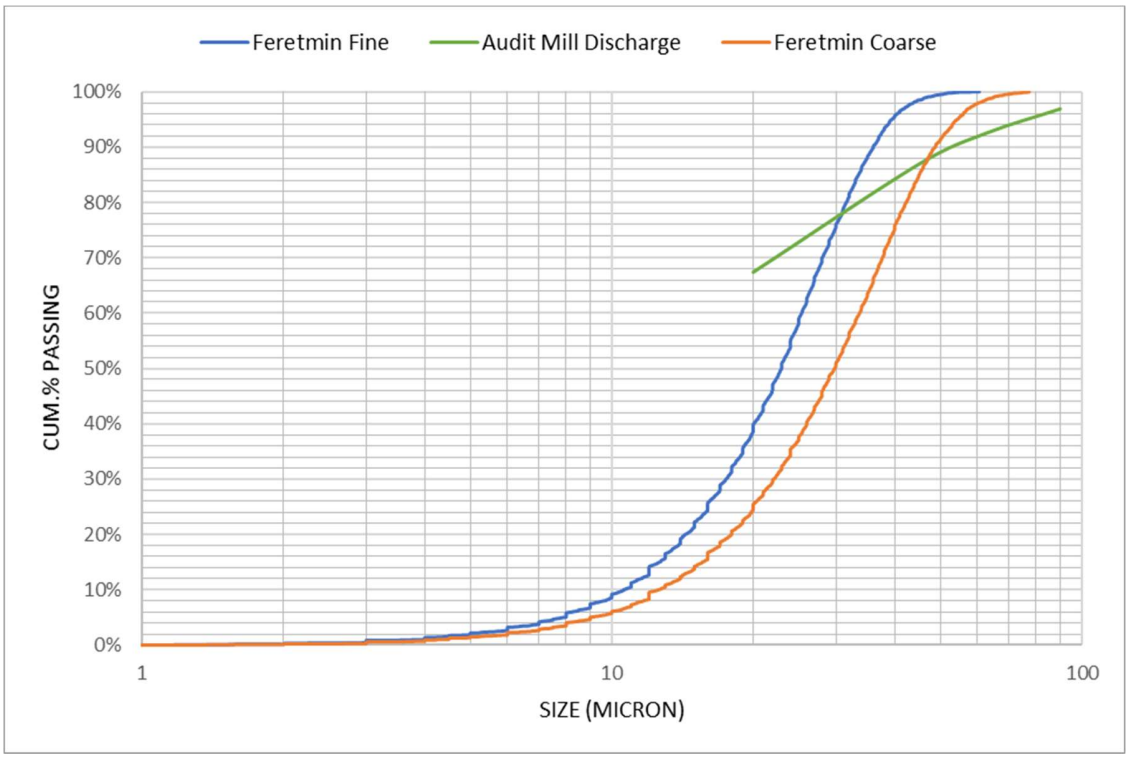

Figure 33 : Comparison of particle size distribution curves for different Voronoi tessellation net size

To test the effect of the Voronoi tessellation grid or net size a coarser grind was simulated, 80% passing 41 microns. As can be seen in Figure 33 this resulted in a coarser size distribution. Assessing the difference in the audit and tessellation curve slopes the issue may not be the breakage but the particle flow through an open circuit SMD. Due to the mode of the flow through the SMD around 15% of the feed will pass through the mill, bypassing the grinding zone, this resulting in no or limited grinding of this proportion of the feed. To improve the simulated mill output it may be necessary to model the flow in the SMD and then allow for the lack of breakage in a proportion of the feed. Alternatively, a change could be made in the Voronoi tessellation grid to increase the ratio of smaller cells. The top size could then be adjusted to a coarser size without affecting the targeted 80% passing size. However, this would be more complicated and

would need to be adjusted for different mill or circuit types with different values of slurry or flow bypass.

Liberation data was also generated using the tessellation particles generated during the simulated breakage both for the fine tessellation grid and the coarse tessellation grid. The simulated breakage liberation data was compared to the liberation data from the QEMSCAN analysis. This would give a good prediction of the expected performance of a downstream enrichment process.

Table 16 : Boliden Garpenberg Zinc SMD Mill Discharge Fine Tessellation Simulated Liberation Data

Mass	Liberation of Sphalerite (ZnS)									
%	<=10	<=20	<=30	<=40	<=50	<=60	<=70	<=80	<=90	<=100
	0.2	0.3	0.4	0.6	0.8	1.1	1.5	2.4	4.9	87.8

Table 17 : Boliden Garpenberg Zinc SMD Mill Discharge Coarse Tessellation Simulated Liberation Data

Mass	Liberation of Sphalerite (ZnS)									
%	<=10	<=20	<=30	<=40	<=50	<=60	<=70	<=80	<=90	<=100
	0.2	0.4	0.4	0.6	1.0	1.2	1.6	2.7	6.1	85.8

Table 18 : Boliden Garpenberg Zinc SMD Mill Discharge Audit Liberation Data

Mass	Liberation of Sphalerite (ZnS)									
%	<=10	<=20	<=30	<=40	<=50	<=60	<=70	<=80	<=90	<=100
	0.6	0.8	0.9	1.0	1.6	1.5	2.0	3.3	6.7	81.6

Comparing the data for the fine Voronoi tessellation grid in Table 16 with the coarse tessellation grid in Table 17 the coarser grid has generated less liberation of the locked particles than the fine grid. This shows that by adjusting the size or area of the Voronoi tessellation cells it is possible to adjust the particle size distribution produced and the liberation data of the fractured particles. The effect is also as expected in that a fine tessellation or fracture has liberated more of the locked particles.

As can be seen from simulated data in Tables 16 and 17 when compared to the QEMSCAN data as expected based on the size distribution data the sphalerite liberation is significantly higher for the tessellation data than the audit data. The reason for the higher liberation value is the finer top size of the tessellation particle size distribution compared to the audit mill discharge size distribution. The maximum particle size in the tessellation data is approximately 50 microns this compares to the audit data that shows 10% of the particles are larger than 50 microns.

Conclusions

The aim of the study was to investigate three regrind circuits at two different mineral processing operations, to determine if it was possible to simulate the regrind circuit product size distribution and mineralogy and then determine the effect on the downstream enrichment process.

Two approaches were used for the Northlands iron ore sample collected during the plant audit, the first involved small-scale laboratory tests and the second digitization of the particles followed by simulated breakage and enrichment.

Laboratory grinding tests showed a good correlation between the jar mill product size distribution curve and the Northlands audit hydrocyclone overflow size distribution.

The Davis tube testwork showed a good correlation between the Northlands concentrator audit LIMS separator sample and the Davis tube concentrate and tailings samples for both the iron assays and iron recovery.

Analysis of the Northlands audit LIMS concentrate and tailings samples showed that the LIMS design has insufficient turbulence to break the agglomerates allowing ultrafine gangue to report to the magnetic concentrate. A change to the water addition or separating the drum stages and including inter-stage mixing may improve the breaking of the magnetic agglomerates.

The tessellation breakage simulation on the Northlands regrind circuit feed provided excellent results. The mill discharge size distribution curve generated by the tessellation process matched the audit size distribution closely, which is vital for the subsequent mineralogical data to be valid. The concentrate iron grade differed by only

0.1% between the tessellation simulated value and the iron assay from the QEMSCAN analysis. The concentrate recovery showed a difference of only 0.5%.

The Boliden Garpenberg regrind audit results indicate that the CuPb regrind circuit has a significant effect on the grade and recovery of the valuable minerals, the zinc regrind has limited effect on both grade and recovery, this reflects the experience of the concentrator operation.

The laboratory flotation tests conducted on the CuPb regrind circuit showed good reproducibility. The laboratory flotation tests conducted on the zinc regrind circuit also showed good reproducibility.

The flotation tests on the CuPb SMD regrind mill feed and mill discharge showed a good improvement in the flotation performance after regrinding. The laboratory SMD tests correlated well with the zinc audit data, but less well with the CuPb audit with a deviation in the product size distribution curve slope at the finer end of the curve.

The Boliden Garpenberg zinc regrind tessellation data showed a poor correlation for the size distribution curve generated from the breakage data, compared to the audit size distribution data.

The liberation of the valuable and gangue minerals simulated during the tessellation process is linked to the size distribution of the tessellation breakage particles, therefore the liberation data also showed a poor correlation.

Acknowledgements

I would like to thank my thesis supervisors Dr. Richard Pascoe and Prof. Hylke Glass for support during the Masters project. Thanks also to John Trescot who persuaded me to conduct the testwork and persuaded Metso to fund the thesis preparation.

A special mention should also be made to Northlands Resources and Boliden Garpenberg for allowing the regrind circuits to be sampled and the support provided during the sampling campaigns, especially Henrik Lindvall, Stellan Sundberg and Jaakko Larkomaa. For the QEMSCAN analysis of the samples and data analysis of the results thanks to Dr. Gavyn Rollinson and Dr. Klass van der Wielen.

Finally, to my wife Sarah, for proof reading and her never ending support during the trips away and preparation of the report.

Bibliography

Baker, H. and Lepley, B. (2010), 'Mineral resource estimate for the Tapuli iron deposit', (Pajala municipality, Norrbotten County, Sweden: SRK Consulting), 178-79.

Bolin, N. J. and Norén, P. (1992), 'Use of reagents in Boliden Mineral AB', *Minerals Engineering,* 5 (3), 311-16.

Bradshaw, D. J. and Vos, F. (2013), 'The development of a small scale test for rapid characterisation of flotation response (JKSMI)', *45th Annual Meeting of the Canadian Mineral Processors Conference* (Ottawa, ON. Canada), 43-57.

Davey, G. (2002), 'Ultrafine and fine grinding using the Metso Stirrd media Detritor (SMD)', *34th Annual Meeting of the Canadian Mineral Processors* (Ottawa, ON, Canada), 153-70.

Dobrin, Adam (2005), *A Review of Properties and Variations of Voronoi Diagrams* (Whitman College: Whitman College).

Dworzanowski, M. (2012), 'Maximizing the recovery of fine iron ore using magnetic separation', *The Journal of The Southern African Institute of Mining and Metallurgy,* 112, 197-202.

Ersayin, Salih (2004), 'Low intensity magnetic separator modelling: a pseudo liberation approach', *Mineral Processing and Extractive Metallurgy,* 113 (3), 167-74.

Harper, P. (2008), 'What Does a Feasibility Study Cost?', *International Mining*, April 2008, 60.

Johnson, N. W. (2006), 'Liberated 0–10μm particles from sulphide ores, their production and separation—Recent developments and future needs', *Minerals Engineering,* 19 (6-8), 666-74.

Kloln, S., Stephenson, D., and Granados, H. (2016), 'Constancia Project Process Plant Design and Start Up', *48th Canadian Mineral Processors*, 100-12.

Lichter, J.K.H. and Davey, G. (2002), 'Selection and Sizing of Ultrafine and Stirred Grinding Mills', in A.L. Mular, D.H. Halbe, and D.J. Barratt (eds.), *Mineral Processing Plant Design, Practice and Control* (1: SME), 783-800.

Lishchuk, Viktor, Lamberg, Pertti, and Lund, Cecilia (2016), 'Evaluation of sampling in geometallurgical programs through synthetic deposit model', *XXVIII International Mineral Processing Congress, Québec City, September 11-15 2016*.

Mazzinghy, D. , et al. (2017), 'Vertical Stirred Mill Scaleup and Simulation: Model Validation by Industrial Samplings Results', *Minerals Engineering,* 103-104, 127-33.

McIvor, R. (2014), 'Plant performance improvements using grinding circuit “classification system effciency”', *Mining Engineering*, 66 (9), 67-71.

Metso (2010), 'Metso Test Laboratory - Jar Mill Report'.

Murariu, V. and Svoboda, J. (2003), 'The Applicability of Davis Tube tests to Ore Separation by Drum Magnetic Separators', *Physical Separation in Science and Engineering,* 12 (1), 1-11.

Parian, Mehdi, Lamberg, Pertti, and Rosenkranz, Jan (2016), 'Developing a particle-based process model for unit operations of mineral processing – WLIMS', *International Journal of Mineral Processing,* 154 (Supplement C), 53-65.

Pascoe, R.D., Rollinson, G., and Davey, G. (2015), 'Investigation of the Performance of a low intensity magnetic separator using QEMSCAN analysis', in B. Wills (ed.), *Minerals Engineering Physical Separation* (Falmouth, UK).

Rollinson, G., et al. (2011), 'Characterisation of non-sulphide zinc deposits using QEMSCAN', *Minerals Engineering,* 24 (8), 778-87.

Runge, K.C., Tabosa, E., and Jankovic, A. (2013), 'Particle Size Distribution Effects that Should be Considered when Performing Flotation Geometallurgical Testing', *The Second AUSIMM International Geometallurgy Conference* (Brisbane).

Sepor (2010), 'Davis Tube Tester Manual'.

van der Wielen, K. P. and Rollinson, G. (2016), 'Texture-based analysis of liberation behaviour using Voronoi tessellations', *Minerals Engineering,* 89, 193-07.

Vassiliev, P.V., Ledoux, H., and Gold, C. (2008), 'Modeling Ore Textures and Mineral Liberation Using 3D Voronoi Diagrams', *Geo Database Management Center* (Delft University).

Vizcarra, T. G., et al. (2011), 'The influence of particle shape properties and associated surface chemistry on the flotation kinetics of chalcopyrite', *Minerals Engineering,* 24 (8), 807-16.

Whiteman, E., Lotter, N. O., and Amos, S. (2015), 'A Practical Process Mineralogy Approach to Advancing the Flowsheet for the Kamoa Project', *MEI Flotation '15* (Cape Town, South Africa).

Wills, B.A. and Finch, J.A. (2016), *Wills' Mineral Processing Technology* (8th edn.: Butterworth-Heinemann).

Wood, K. R. (2002), 'Flotation equipment selection and plant layout', in A.L. Mular, D.H. Halbe, and D.J. Barratt (eds.), *Minerals Processing Plant Design, Practice and Control* (Littleton, CO., USA: SME), 1204-38.

Xiao, Xiao, et al. (2012), 'The liberation effect of magnetite fine ground by vertical stirred mill and ball mill', *Minerals Engineering,* 34 (Supplement C), 63-69.

Appendix A – NRAB regrind circuit QEMSCAN Data

Measure.	CSM Lab Code	4RP21	4RP22	4RP23	4RP24
	Sample Code	1 Tower Mill Feed	2 Tower Mill Product LIMS Feed	3 LIMS Mags	4 LIMS Non-Mags
	Measurement Mode	FieldImage	PMA	PMA	PMA
	No. Particles	42,121	7,055	7,566	5,766
	No. X-ray Analysis Points	1,752,958	221,821	227,912	279,900
	X-ray Pixel Spacing (Microns)	10	1.5	1.5	1.5
	Max Particle Size (Microns)	1046.3	105.9	61.7	139.0
	Min Particle Size (Microns)	15	2.205	2.205	2.205
	Average Particle Size (Microns)	147.7	13.2	12.3	19.6
	Elemental Fe Mass % (calculated)	61.7	61.8	70.2	7.4
Mineral Mass (%)	Magnetite	83.51	83.18	96.65	1.22
	Ilmenite	0.19	0.14	0.16	0.48
	Rutile	0.02	0.04	0.01	0.14
	Titanite	0.03	0.07	0.01	0.08
	Fe sulphides	0.07	0.38	0.08	0.14
	Quartz	0.03	0.03	0.02	0.08
	Feldspar	0.01	0.03	0.03	0.14
	Mica	0.73	0.50	0.05	3.56
	Chlorite	0.10	0.10	0.07	0.32
	Mg silicates	4.36	5.05	0.75	27.89
	Mg Fe silicates	3.80	4.43	1.30	15.96
	Pyroxene/Amphibole	3.90	3.66	0.54	33.36
	Calcite	0.64	0.79	0.03	5.80
	Dolomite/Ankerite	2.39	1.33	0.24	9.70
	Magnesite	0.08	0.20	0.02	0.26
	Apatite	0.09	0.05	0.02	0.73
	Others	0.07	0.04	0.02	0.14
Mineral Volume(%)	Magnetite	73.59	73.01	94.07	0.73
	Ilmenite	0.19	0.13	0.17	0.30
	Rutile	0.02	0.04	0.01	0.10
	Titanite	0.03	0.08	0.01	0.06
	Fe sulphides	0.07	0.36	0.08	0.08

	Quartz	0.04	0.05	0.03	0.09
	Feldspar	0.01	0.05	0.05	0.16
	Mica	1.14	0.78	0.08	3.58
	Chlorite	0.16	0.16	0.12	0.34
	Mg silicates	7.69	8.90	1.48	31.41
	Mg Fe silicates	6.74	7.83	2.54	18.06
	Pyroxene/Amphibole	5.18	4.82	0.79	28.14
	Calcite	1.07	1.31	0.05	6.15
	Dolomite/Ankerite	3.75	2.06	0.41	9.77
	Magnesite	0.12	0.29	0.03	0.25
	Apatite	0.13	0.07	0.03	0.65
	Others	0.07	0.05	0.03	0.13
Grain Size	Magnetite	105.5	10.8	11.7	5.2
(AVG Microns)	Ilmenite	20.7	5.0	5.8	8.3
	Rutile	15.7	4.3	3.3	3.5
	Titanite	19.7	9.9	4.0	7.0
	Fe sulphides	18.3	8.8	3.2	4.7
	Quartz	20.5	4.6	4.5	4.9
	Feldspar	19.2	4.1	5.1	6.7
	Mica	37.7	6.6	2.8	9.3
	Chlorite	15.6	2.6	2.7	2.9
	Mg silicates	49.6	10.3	8.5	8.9
	Mg Fe silicates	24.1	5.7	4.4	5.5
	Pyroxene/Amphibole	53.2	10.4	5.9	10.7
	Calcite	37.2	12.8	3.5	9.5
	Dolomite/Ankerite	61.0	10.9	6.9	12.9
	Magnesite	32.7	15.1	8.3	7.9
	Apatite	45.9	6.3	4.9	13.4
	Others	39.3	2.9	3.6	3.9

Appendix B – Boliden Garpenberg QEMSCAN Data

Measurement	CSM Lab Code	17RP11	17RP12	17RP13	17RP14	17RP15	17RP16	17RP17	17RP18	17RP19	17RP1A
	Sample ID	Cyclone Feed +38	Cyclone Feed -38	Cyclone u/f +38	Cyclone u/f -38	Cyclone o/f	Mill discharge whole	MP Cleaner	Return to Rougher Whole	Scavenger Conc +38	Scavenger Conc -38
	Measurement Mode	PMA	PMA	PMA	PMA	PMA	PMA	PMA	PMA	PMA	PMA
	No. Particles	10,207	12,425	8,602	12,326	12,512	10,991	12,439	10,365	9,505	12,096
	No. X-ray Analysis Points	886732	198016	1007859	395352	183343	136984	222656	124940	911643	158978
	X-ray Pixel Spacing	4	1.5	4	1.5	1.5	2	1.5	2	4	1.5
	AVG Particle Long Axis (Microns)	44.4	7.7	54.6	10.0	7.2	7.8	7.6	7.2	46.1	7.0
	AVG Particle Short Axis (Microns)	27.9	4.9	35.0	6.5	4.7	5.2	4.8	4.8	28.5	4.5
	AVG Size (Horiz) Microns	52.0	9.0	56.0	13.4	8.5	11.8	9.7	11.8	54.3	7.4
	Min Size (Horiz) Microns	5.6	2.2	5.6	2.2	2.2	2.9	2.2	2.9	5.6	2.2
	Max Size (Horiz) Microns	301.6	52.1	259.4	59.3	51.0	103.0	91.3	158.6	222.2	39.7
Elemental Mass (%)	Cu	0.07	0.29	0.17	0.15	0.28	0.08	0.20	0.23	0.16	0.34
(Calculated)	Pb	6.54	21.82	6.73	16.21	19.86	8.06	18.08	14.76	5.69	21.97

	Zn	25.62	16.95	27.64	24.07	14.14	26.84	15.78	15.61	22.34	16.48
Mineral Mass(%)	Sphalerite	38.83	25.93	41.91	36.65	21.62	41.09	24.03	23.79	33.84	25.19
(Density weighted)	Chalcopyrite	0.22	0.79	0.49	0.43	0.86	0.24	0.54	0.67	0.46	0.93
	Friebergite	0.02	0.03	0.03	0.02	0.01	0.01	0.04	0.01	0.08	0.01
	Galena	7.56	25.19	7.78	18.72	22.91	9.16	20.87	17.02	6.57	25.37
	Pyrite	22.80	8.47	22.75	20.40	7.07	26.85	7.11	9.86	27.92	8.19
	Pyrrhotite	0.96	0.86	1.16	1.85	0.40	2.99	0.72	0.87	0.81	0.57
	Arsenopyrite	0.27	0.52	0.32	0.61	0.20	0.24	0.18	0.19	0.24	0.28
	Acanthite	0.30	0.11	0.20	0.10	0.09	0.04	0.11	0.06	0.17	0.14
	Molybdenite	0.06	0.64	0.11	0.36	0.56	0.22	0.48	0.39	0.05	0.79
	Alabandite	0.15	0.16	0.18	0.21	0.14	0.07	0.13	0.17	0.14	0.23
	Ti minerals	0.01	0.03	0.02	0.02	0.05	0.01	0.02	0.02	0.01	0.01
	Fe-Ox/CO3	0.19	0.50	0.17	0.45	0.56	0.41	0.33	0.42	0.09	0.37
	Quartz	9.88	4.52	10.45	2.09	4.62	6.00	5.01	8.92	11.04	3.64
	K-feldspar	0.57	0.37	0.72	0.52	0.66	0.47	0.46	2.12	0.87	0.37
	Plagioclase feldspar	0.77	0.58	0.86	0.60	0.57	0.77	0.54	1.29	0.78	0.76
	Muscovite	0.36	0.34	0.24	0.22	0.41	0.19	0.62	1.39	0.42	0.16

	Phlogopite	0.38	0.43	0.28	0.16	0.74	0.13	0.44	1.24	0.38	0.24
	Chlorite	1.17	4.34	0.76	1.86	4.33	1.24	3.71	2.66	1.17	3.77
	Kaolinite	0.00	0.01	0.02	0.03	0.01	0.01	0.00	0.04	0.00	0.00
	Mg silicates	9.32	21.03	5.32	9.96	28.46	6.40	26.29	16.28	7.94	23.37
	Ca Mg silicates	3.04	2.08	3.41	2.18	2.74	0.97	4.32	2.27	3.15	2.62
	Ca Mg Mn silicates	0.25	0.14	0.21	0.17	0.09	0.14	0.30	0.15	0.26	0.21
	Ca Fe Mg silicates	0.61	1.06	0.56	0.39	1.21	0.36	1.29	0.66	0.80	1.25
	Epidote Group/Garnet	0.12	0.10	0.12	0.09	0.12	0.08	0.11	0.15	0.14	0.17
	Mn silicates/Garnet	0.60	0.15	0.69	0.54	0.21	0.22	0.44	0.28	0.64	0.35
	Sauconite	0.06	0.02	0.04	0.01	0.01	0.05	0.07	0.03	0.03	0.03
	Calcite	0.61	0.62	0.47	0.58	0.68	0.40	1.14	6.90	0.77	0.60
	Dolomite	0.77	0.91	0.67	0.62	0.57	1.16	0.65	2.08	1.11	0.26
	Apatite	0.03	0.03	0.02	0.00	0.01	0.00	0.01	0.01	0.01	0.00
	Fluorite	0.06	0.04	0.04	0.10	0.01	0.03	0.01	0.03	0.07	0.00
	Zircon	0.00	0.00	0.00	0.00	0.01	0.00	0.00	0.00	0.02	0.01
	Others	0.01	0.02	0.02	0.07	0.03	0.06	0.03	0.02	0.01	0.07
Mineral Volume (%)	Sphalerite	39.21	29.65	43.23	41.75	23.70	47.77	25.04	24.66	34.12	28.90

(area %)	Chalcopyrite	0.26	0.87	0.52	0.52	0.93	0.29	0.58	0.72	0.50	1.04
	Friebergite	0.01	0.02	0.02	0.01	0.01	0.01	0.03	0.00	0.06	0.00
	Galena	4.72	16.04	4.98	12.51	14.20	5.93	12.99	10.33	4.18	16.18
	Pyrite	16.54	6.12	16.67	15.22	5.12	19.11	5.13	6.89	20.50	5.94
	Pyrrhotite	0.75	0.61	0.92	1.48	0.28	2.23	0.51	0.61	0.65	0.40
	Arsenopyrite	0.16	0.28	0.19	0.37	0.10	0.14	0.09	0.10	0.14	0.15
	Acanthite	0.15	0.05	0.10	0.05	0.04	0.02	0.05	0.03	0.09	0.06
	Molybdenite	0.04	0.38	0.07	0.24	0.33	0.14	0.28	0.23	0.03	0.47
	Alabandite	0.14	0.13	0.16	0.19	0.11	0.06	0.10	0.14	0.13	0.19
	Ti minerals	0.01	0.02	0.02	0.01	0.03	0.01	0.02	0.02	0.01	0.01
	Fe-Ox/CO3	0.16	0.41	0.14	0.42	0.45	0.35	0.26	0.34	0.07	0.30
	Quartz	13.60	5.65	14.55	2.92	5.62	7.88	6.20	10.97	15.39	4.52
	K-feldspar	0.81	0.47	1.03	0.75	0.82	0.63	0.59	2.67	1.24	0.47
	Plagioclase feldspar	1.03	0.71	1.16	0.82	0.68	0.98	0.66	1.57	1.05	0.92
	Muscovite	0.47	0.39	0.31	0.28	0.47	0.23	0.71	1.59	0.55	0.19
	Phlogopite	0.47	0.50	0.35	0.20	0.84	0.16	0.49	1.41	0.49	0.28
	Chlorite	1.58	5.37	1.05	2.58	5.20	1.60	4.53	3.23	1.60	4.62
	Kaolinite	0.00	0.01	0.02	0.03	0.01	0.01	0.00	0.05	0.00	0.00

	Mg silicates	12.96	26.68	7.47	14.13	35.09	8.49	32.98	20.30	11.19	29.43
	Ca Mg silicates	3.22	2.01	3.66	2.36	2.57	0.98	4.12	2.15	3.39	2.51
	Ca Mg Mn silicates	0.30	0.16	0.25	0.21	0.10	0.16	0.33	0.16	0.32	0.23
	Ca Fe Mg silicates	0.78	1.33	0.74	0.54	1.48	0.46	1.61	0.79	1.01	1.59
	Epidote Group/Garnet	0.12	0.10	0.13	0.10	0.11	0.08	0.11	0.14	0.15	0.17
	Mn silicates/Garnet	0.54	0.13	0.62	0.49	0.17	0.19	0.36	0.22	0.57	0.28
	Sauconite	0.07	0.02	0.06	0.01	0.02	0.06	0.09	0.04	0.05	0.04
	Calcite	0.80	0.77	0.62	0.79	0.82	0.52	1.37	8.23	1.01	0.73
	Dolomite	0.98	1.05	0.86	0.80	0.64	1.41	0.74	2.36	1.42	0.30
	Apatite	0.03	0.03	0.02	0.00	0.01	0.00	0.01	0.01	0.01	0.00
	Fluorite	0.07	0.05	0.04	0.12	0.01	0.03	0.01	0.03	0.09	0.00
	Zircon	0.00	0.00	0.00	0.00	0.01	0.00	0.00	0.00	0.01	0.01
	Others	0.01	0.02	0.02	0.09	0.03	0.07	0.03	0.02	0.01	0.06
Grain Size	Sphalerite	51.3	10.4	48.4	15.8	8.9	9.9	11.3	11.1	51.3	8.0
(Average Microns)	Chalcopyrite	15.0	5.7	20.9	6.5	5.3	5.9	4.9	6.7	23.7	4.5
	Friebergite	9.1	4.1	13.0	4.6	3.7	4.1	5.1	3.5	21.6	2.2

	Galena	18.3	5.8	18.1	7.9	5.0	6.5	5.2	5.9	17.4	4.3
	Pyrite	49.8	5.5	45.3	14.1	4.3	8.0	5.0	6.7	53.0	4.6
	Pyrrhotite	35.9	8.4	34.2	15.5	6.1	22.1	9.6	12.1	32.0	6.1
	Arsenopyrite	23.4	5.7	26.5	10.5	2.7	4.2	2.8	3.2	23.5	2.3
	Acanthite	17.0	4.5	14.3	5.0	3.5	4.8	3.7	4.1	10.0	3.5
	Molybdenite	6.2	2.4	8.9	2.7	2.2	3.3	2.3	3.1	5.8	2.4
	Alabandite	11.4	6.3	11.5	6.0	4.6	3.7	4.4	6.6	11.5	5.2
	Ti minerals	9.0	3.5	14.4	5.1	4.9	3.7	4.1	4.8	9.3	3.1
	Fe-Ox/CO3	15.1	6.0	16.8	5.0	6.2	5.3	4.1	5.5	11.1	4.4
	Quartz	55.7	5.3	57.0	6.9	4.7	13.4	5.9	10.5	59.6	3.8
	K-feldspar	22.1	3.8	30.7	10.3	5.2	7.2	4.4	11.5	26.9	4.3
	Plagioclase feldspar	22.9	7.1	24.5	12.1	6.2	10.9	7.2	10.3	24.2	9.4
	Muscovite	21.4	5.0	19.6	7.0	5.8	8.4	8.0	11.6	21.3	4.6
	Phlogopite	15.6	4.0	17.9	4.2	4.9	4.7	4.0	8.9	17.1	3.6
	Chlorite	8.2	2.9	9.0	2.9	2.7	4.0	2.9	3.6	8.7	2.7
	Kaolinite	7.1	3.9	23.6	5.2	2.6	3.1	3.7	8.9	5.6	2.2
	Mg silicates	19.8	6.1	24.5	6.8	6.7	9.1	7.4	7.7	18.7	5.6
	Ca Mg silicates	27.8	6.2	29.5	8.5	6.7	7.3	8.6	7.3	26.7	6.3
	Ca Mg Mn silicates	10.6	3.9	9.8	4.5	2.9	4.7	4.0	4.7	10.8	5.5

	Ca Fe Mg silicates	8.9	2.6	9.2	2.5	2.6	3.3	3.3	3.3	10.6	2.5
	Epidote Group/Garnet	12.1	3.6	11.2	5.6	3.2	4.0	3.9	5.5	12.3	5.2
	Mn silicates/Garnet	19.1	3.5	20.2	9.2	4.1	4.4	8.6	7.2	22.6	6.3
	Sauconite	9.7	2.4	9.4	2.4	2.3	3.2	2.8	3.4	7.2	2.4
	Calcite	29.5	5.4	29.9	9.5	5.5	6.5	8.9	39.6	36.0	6.2
	Dolomite	41.1	8.6	42.2	11.0	6.0	17.6	7.3	14.9	54.4	5.6
	Apatite	31.4	7.0	35.9	4.2	4.4	2.9	4.1	4.7	12.9	2.2
	Fluorite	22.0	5.2	24.2	11.7	3.3	6.5	3.3	4.0	19.9	2.6
	Zircon	12.7	0.0	11.3	5.1	5.7	2.9	3.3	2.9	32.8	8.8
	Others	11.2	3.0	9.6	7.3	3.4	5.0	3.0	3.1	6.5	3.9

Appendix C – Boliden Garpenberg Zinc Regrind QEMSCAN Data

Measurement	CSM Lab Code	15RP11	15RP12	15RP13	15RP14	15RP15	15RP16	15RP17	15RP18	15RP19	15RP1A
	Sample ID	Zn Cyc. Feed +38	Zn Scav. Conc +38	Zn Mp Cleaner +38	Zn Cyc. U/F +38	Zn Cyc. Feed -38	Zn Cyc. U/F -38	Zn Scav.Conc -38	Zn Mp Cleaner -38	Zn Mill Disc Whole	Zn Cyc. O/F Whole
	Measurement Mode	PMA	PMA	PMA	PMA	PMA	PMA	PMA	PMA	PMA	PMA
	No. Particles	6195	6485	6822	6127	5927	5752	6031	6408	6414	5791
	No. X-ray Analysis Points	1147309	1464014	1053259	1764319	123126	935004	144743	161477	204212	136021
	X-ray Pixel Spacing	3	3	3	3	1	1.5	1	1	1	1
	AVG Particle Long Axis (Microns)	44.4	52.9	43.0	59.8	5.4	24.7	5.7	6.3	6.9	5.6
	AVG Particle Short Axis (Microns)	27.0	31.7	25.7	36.6	3.6	15.3	3.8	4.0	4.7	3.6
	AVG Size (Horiz) Microns	65.6	67.4	57.0	75.2	6.1	26.3	6.9	6.8	7.4	6.8
	Min Size (Horiz) Microns	4.4	4.4	4.4	4.4	1.4	2.2	1.4	1.4	1.4	1.4
	Max Size (Horiz) Microns	276.3	320.6	222.9	241.8	38.8	83.8	40.3	29.2	36.2	53.1

Elemental Mass (%)	Cu	0.03	0.03	0.09	0.05	0.18	0.01	0.07	0.02	0.03	0.05
	Pb	0.60	0.57	0.80	0.47	4.37	0.82	4.31	3.15	0.73	3.74
	Zn	47.52	48.07	24.33	49.12	15.46	14.49	19.85	5.63	38.19	15.36
Mineral Mass(%)	Sphalerite	71.99	72.83	36.78	74.39	23.81	21.91	30.53	8.70	58.76	23.61
	Chalcopyrite	0.11	0.10	0.28	0.17	0.51	0.19	0.35	0.13	0.08	0.13
	Galena	0.68	0.64	0.90	0.54	4.89	0.95	4.79	3.56	0.56	4.20
	Pyrite	12.85	10.58	31.97	13.74	23.94	43.71	23.57	29.27	25.72	21.24
	Pyrrhotite	3.58	3.16	9.85	2.37	9.23	25.39	5.76	7.89	4.05	8.22
	Arsenopyrite	0.07	0.04	0.04	0.09	0.29	1.18	0.14	0.28	0.13	0.24
	Ti minerals	0.01	0.03	0.02	0.02	0.04	0.02	0.03	0.06	0.01	0.02
	Fe-Ox/CO3	0.15	0.16	0.20	0.13	0.57	0.64	0.76	0.49	0.28	0.74
	Gahnite spinel	0.01	nd	0.23	0.01	0.02	0.13	nd	0.01	0.01	nd
	Quartz	3.50	2.79	4.58	2.39	7.55	0.80	5.15	10.13	2.50	5.70
	K-feldspar	0.35	0.77	1.47	0.41	0.90	0.15	0.53	1.17	0.79	1.25
	Plagioclase feldspar	0.29	0.50	1.14	0.40	0.86	0.23	0.88	1.34	0.40	1.19
	Biotite	0.07	0.07	0.14	0.11	0.08	0.02	0.05	0.35	0.09	0.06
	Muscovite	0.21	0.48	0.64	0.29	0.97	0.09	0.49	0.98	0.36	0.87
	Phlogopite	0.12	0.50	0.24	0.37	0.68	0.02	0.48	1.13	0.05	0.51
	Chlorite	0.62	0.60	1.16	0.49	3.18	0.29	2.88	4.90	0.75	3.60
	Kaolinite	<0.01	<0.01	<0.01	<0.01	0.03	0.02	0.01	<0.01	0.01	0.05
	Ca Mg silicates	2.30	3.66	3.80	2.23	4.09	1.47	2.91	6.43	1.73	3.03
	Ca Fe Mg silicate	0.37	0.41	0.50	0.22	1.16	0.22	1.12	1.70	0.26	1.34
	Mg silicates	1.54	1.10	3.24	0.43	14.13	1.05	15.67	17.64	1.45	20.58
	Mn silicates	0.34	0.46	0.62	0.19	0.32	0.69	0.29	0.53	0.17	0.30

	Calcite	0.24	0.39	0.56	0.47	0.92	0.26	0.78	1.12	0.79	1.29
	Dolomite	0.50	0.66	1.43	0.45	1.04	0.38	2.12	1.78	0.79	1.15
	Apatite	0.03	0.02	0.02	<0.01	0.01	0.03	0.01	0.01	<0.01	0.01
	Fluorite	<0.01	0.02	0.08	0.02	0.02	0.02	0.01	0.01	0.03	0.01
	Zircon	nd	<0.01	<0.01	<0.01	<0.01	0.03	<0.01	0.01	nd	<0.01
	Others	0.05	0.04	0.09	0.07	0.75	0.13	0.68	0.37	0.23	0.67
Mineral Volume(%)	Sphalerite	72.87	73.06	39.10	75.80	28.37	26.84	34.97	11.13	67.91	26.97
	Chalcopyrite	0.14	0.13	0.31	0.20	0.53	0.21	0.31	0.12	0.09	0.15
	Galena	0.46	0.42	0.62	0.36	3.16	0.74	3.05	2.25	0.35	2.66
	Pyrite	9.67	7.86	24.61	10.38	17.42	38.05	16.84	21.53	16.81	15.05
	Pyrrhotite	2.90	2.53	8.21	1.94	6.51	23.99	4.03	5.60	2.80	5.68
	Arsenopyrite	0.04	0.03	0.03	0.06	0.15	0.85	0.07	0.15	0.07	0.12
	Ti minerals	0.01	0.02	0.02	0.02	0.03	0.03	0.03	0.05	0.01	0.02
	Fe-Ox/CO3	0.14	0.15	0.19	0.13	0.46	0.70	0.60	0.41	0.23	0.59
	Gahnite spinel	0.01	nd	0.21	<0.01	0.02	0.13	nd	0.01	<0.01	nd
	Quartz	4.97	3.93	6.71	3.44	9.36	1.33	6.32	12.61	3.03	6.92
	K-feldspar	0.51	1.11	2.20	0.61	1.14	0.25	0.67	1.49	0.99	1.55
	Plagioclase feldspar	0.38	0.66	1.54	0.53	0.94	0.33	0.97	1.53	0.44	1.33
	Biotite	0.08	0.08	0.18	0.14	0.08	0.03	0.05	0.37	0.09	0.06
	Muscovite	0.28	0.63	0.87	0.39	1.11	0.14	0.56	1.13	0.40	0.98
	Phlogopite	0.16	0.66	0.33	0.50	0.79	0.03	0.55	1.32	0.05	0.58
	Chlorite	0.86	0.82	1.65	0.68	3.89	0.47	3.49	6.04	0.89	4.30
	Kaolinite	<0.01	<0.01	0.01	<0.01	0.04	0.03	0.01	0.01	0.01	0.05
	Ca Mg silicates	2.53	4.01	4.36	2.50	3.93	1.91	2.77	6.21	1.64	2.85
	Ca Fe Mg silicate	0.43	0.47	0.60	0.26	1.17	0.29	1.13	1.75	0.26	1.32

	Mg silicates	2.19	1.56	4.77	0.59	17.71	1.72	19.52	22.19	1.78	25.30
	Mn silicates	0.31	0.41	0.59	0.18	0.27	0.72	0.23	0.45	0.14	0.24
	Calcite	0.33	0.51	0.77	0.64	1.16	0.41	0.98	1.35	0.93	1.55
	Dolomite	0.66	0.85	1.93	0.60	1.18	0.58	2.40	2.05	0.88	1.29
	Apatite	0.04	0.02	0.02	<0.01	0.01	0.05	0.01	0.01	<0.01	0.01
	Fluorite	<0.01	0.02	0.09	0.02	0.02	0.03	0.01	0.01	0.03	0.01
	Zircon	nd	<0.01	<0.01	<0.01	<0.01	0.02	<0.01	0.01	nd	<0.01
	Others	0.04	0.03	0.07	0.05	0.53	0.12	0.41	0.23	0.16	0.41
Grain Size	Sphalerite	64.4	64.9	56.0	70.6	5.1	26.1	5.9	4.9	6.5	5.3
(AVG Microns)	Chalcopyrite	10.6	9.2	23.0	15.5	5.0	10.9	5.5	3.7	3.0	3.4
	Galena	10.0	11.4	12.1	12.5	2.6	8.2	2.6	3.7	2.0	2.6
	Pyrite	35.0	36.3	45.1	49.3	3.3	19.9	3.7	3.9	3.9	3.5
	Pyrrhotite	38.1	40.1	43.3	36.0	9.0	22.6	7.3	8.0	4.4	9.6
	Arsenopyrite	22.4	13.8	10.1	34.3	3.4	24.0	2.2	5.0	6.4	2.6
	Ti minerals	8.0	17.2	7.6	12.7	2.0	6.4	2.7	2.4	4.5	1.8
	Fe-Ox/CO3	8.0	7.9	7.9	7.5	3.3	6.8	4.2	4.2	2.8	4.9
	Gahnite spinel	16.7	nd	48.4	25.7	6.3	19.4	nd	3.1	2.6	nd
	Quartz	44.0	46.9	39.5	42.1	3.9	15.5	3.3	4.7	6.6	3.4
	K-feldspar	23.0	27.2	29.4	25.3	3.3	12.8	3.1	4.0	6.0	4.5
	Plagioclase feldspar	16.1	20.5	22.1	18.6	3.1	8.6	3.9	3.9	4.5	4.1
	Biotite	7.3	5.8	6.3	6.5	1.9	3.6	1.8	2.3	1.8	1.7
	Muscovite	11.8	17.4	12.9	14.6	2.8	5.5	2.2	2.4	2.5	2.5
	Phlogopite	10.4	29.4	11.2	20.2	2.9	4.4	2.6	2.7	3.2	2.3
	Chlorite	8.6	8.9	9.0	11.0	2.0	3.9	1.9	2.1	2.7	2.0
	Kaolinite	6.8	5.4	5.3	6.3	2.9	6.4	3.2	2.4	2.2	6.2
	Ca Mg silicates	30.2	34.8	33.9	34.6	4.7	12.6	4.3	4.5	6.0	4.4

	Ca Fe Mg silicate	7.0	6.7	6.9	5.8	1.8	3.2	1.7	1.7	1.7	1.8
	Mg silicates	12.8	12.5	14.6	10.4	3.6	9.1	4.1	4.1	3.3	4.9
	Mn silicates	24.1	26.1	15.9	14.2	3.3	16.9	3.5	3.4	2.6	3.0
	Calcite	33.9	35.5	28.8	37.3	3.0	8.4	3.1	5.0	4.5	3.4
	Dolomite	58.3	51.1	45.6	72.3	3.9	19.6	8.0	5.1	6.9	5.0
	Apatite	46.0	21.8	15.4	8.3	2.1	13.8	3.2	2.1	1.4	1.6
	Fluorite	9.5	14.2	32.3	18.5	1.8	4.8	2.4	1.6	1.6	1.4
	Zircon	nd	7.0	6.6	12.3	1.4	24.6	1.4	3.2	nd	2.9
	Others	5.9	5.7	7.4	8.0	2.0	4.6	1.7	2.0	2.4	1.7